

ENERGETICS AND DYNAMICS OF RESONANT AND NONRESONANT SCATTERING
IN STRONG MAGNETIC FIELDS

DON Q. LAMB AND JOHN C. L. WANG

Department of Astronomy and Astrophysics and the Enrico Fermi Institute, University of Chicago

AND

IRA M. WASSERMAN

Center for Radiophysics and Space Research, Cornell University

Received 1990 January 15; accepted 1990 May 8

ABSTRACT

We present results for the cooling and heating that arise from cyclotron resonant and nonresonant scattering by photons injected into a planar slab plasma of thickness N_e electrons cm^{-2} that is threaded by a superstrong field (B) oriented parallel to the slab normal. From a balance of the cooling and heating, we calculate the equilibrium temperature T_C as a function of field strength B and column depth through the slab. We obtain analytic expressions for T_C for both beamed and isotropic photon injection in the optically thin limit. For the optically thick case, we use Monte Carlo simulations to study the values of T_C resulting from isotropic photon injection into the slab plasma. We find that when T_C is determined by the cooling/heating balance due solely to cyclotron resonant scattering T_C/B remains fairly constant for N_e up to $\sim 6 \times 10^{21}$ electrons cm^{-2} in the optically thick regime. This line-dominated region comes to an end when the extra heating from the hard continuum photons (> 100 keV) becomes competitive with the line processes and drives the equilibrium temperature well above the pure line value. With parameters characteristic of GB 880205, we determine the thickness of the line-dominated region to be $\sim 10^{21}$ – 10^{22} electrons cm^{-2} . Using the pure line cooling/heating model for the line-forming region, Wang *et al.* computed theoretical line spectra and compared these spectra with the data from GB 880205. They found good fits to the data for line-forming regions with column depths $\approx (0.6\text{--}1.8) \times 10^{21}$ electrons cm^{-2} . This qualitative agreement between the best-fit thickness of the line-forming layer demanded by the data and the thickness of the line-dominated layer determined in this paper strongly suggests that the line-dominated layer plays an important, if not central, role in the line formation process.

Requiring that the line-enhanced radiation force exerted on the scattering layer be less than the gravitational force binding this layer to the surface of, for example, a neutron star, gives a limiting *magnetic* Eddington luminosity. Strictly speaking, we can find a limit on the spectral flux at the cyclotron lines. Applying this limit to GB 880205 constrains the distance to this burst to be $\lesssim 200$ pc (3σ upper bound) and implies that the total luminosity $L \lesssim 0.3L_E$, where $L_E \approx 1.26 \times 10^{38}$ M/M_\odot (ergs s^{-1}) is the nonmagnetic Eddington limit for an electron-proton plasma. A pair-dominated scattering layer cannot easily be accommodated in our model since the corresponding distance limit would be far smaller, $\lesssim 5$ pc, which is highly unlikely. Both the cyclotron interpretation of line features seen in GB 880205 and the distance limit strongly suggest that this burst originates from a strongly magnetized neutron star in the Galactic disk.

Subject headings: gamma rays: bursts — magnetic fields — plasmas — radiation mechanisms — radiative transfer — stars: neutron

I. INTRODUCTION

Photons impinging on electrons in a plasma permeated by a superstrong magnetic field may engage in single or multiple resonant cyclotron and nonresonant (magnetic continuum) scattering. Each scattering event exchanges energy and momentum between the electrons and photons. The energy exchange is a source of cooling and heating for the plasma, while the momentum exchange gives rise to a line-enhanced radiation force on the scattering plasma. In this paper, we study in detail the energetics, i.e., the cooling and heating, and the dynamics, i.e., the radiation force, resulting from electron-photon resonant (cyclotron) and nonresonant (continuum) scattering in a plasma with magnetic field $B \sim 10^{12}$ G ($\ll B_c = 4.414 \times 10^{13}$ G). We discuss the scattering energetics and the scattering dynamics, in that order, presenting first the case in which the plasma is optically thin to resonant scattering in the cyclotron first harmonic (=fundamental). Precise analytic results can be obtained in the optically thin limit, for which the basic physics is more transparent. We then present the numerical results for the optically thick case and, where possible, semianalytic estimates which aid in visualizing the details and results of the nontrivial radiative transfer physics involved.

We assume the scattering region to be a plane-parallel slab threaded by a uniform superstrong magnetic field oriented parallel to the slab normal and populated by scattering electrons with a (quasi-)thermal distribution of momenta parallel to the field at temperature T . Although the electrons are subject to continual heating by incident photons, they may nevertheless maintain a quasi-thermal distribution (along the field) through their electrostatic coupling to protons (or other heavy ions) which we assume to populate the layer as well. For the distribution of electron momenta orthogonal to the field where the motion is quantized into Landau levels, we assume all electrons to be in the ($n = 0$, $\sigma = -1$) Landau ground state. This is appropriate at sufficiently low

electron densities ($n_e \ll 8 \times 10^{27} B_{12}^{7/2} \text{ cm}^{-3}$) where collisional excitation and de-excitation of higher Landau levels may be ignored (Ventura 1973) and at sufficiently low resonant photon densities where radiative population of higher Landau levels may also be ignored. We assume that the resonant scattering layer is static, thereby ignoring the possibility of significant bulk flow. Suprathermal relative motion between electrons and ions is unstable (e.g., Buneman 1959), and we expect any such relative motions to be suppressed. Overall constant velocity motion of the scattering layer can be accounted for by Lorentz transforming to the rest frame of the plasma. We ignore differential motion in the scattering layer. Substantial, suprathermal *differential* motion is unlikely to be consistent with the relative narrowness of the lines observed in the bursts GB 870303 and GB 880205 (Murakami *et al.* 1988, Fenimore *et al.* 1988; Wang *et al.* 1989), although we cannot entirely rule out the possibility of differential flow at some level.

Quite generally in this paper, we use polarization-averaged photon scattering cross sections, an approximation that is justified at low electron densities ($n_e \ll 10^{22} B_{12}^4 \text{ cm}^{-3}$), where (strong field) vacuum polarization determines the photon propagation modes (see Gnedin, Pavlov, and Shibano 1978). For a slab column density $N_e \equiv N_{e,21} \times 10^{21} \text{ electrons cm}^{-2}$, the optical depth in the cyclotron first harmonic is

$$\tau_1 = 100 N_{e,21} B_{12}^{-1} \left(\frac{T}{\text{keV}} \right)^{-1/2}, \quad (1)$$

where $B = B_{12} \times 10^{12} \text{ G}$ and T is in keV. In contrast, the continuum optical depth is

$$\tau_c \approx \sigma_T N_e = 7 \times 10^{-4} N_{e,21}, \quad (2)$$

where σ_T is the Thomson cross section, and the optical depths in the second and third cyclotron harmonics are

$$\tau_2 = 2.7 N_{e,21} \left(\frac{T}{\text{keV}} \right)^{-1/2}, \quad (3)$$

and

$$\tau_3 = 0.23 N_{e,21} B_{12} \left(\frac{T}{\text{keV}} \right)^{-1/2}. \quad (4)$$

Quite generally, we shall focus on scattering layers that are optically thin in the continuum, but we shall consider a range of values for τ_1 .

In the optically thin case, for which $\tau_1 \ll 1$, we calculate the cooling and heating due to resonant scattering at the cyclotron first harmonic analytically to first order in τ_1 for photons injected with a power-law ($\propto E^{-s}$) energy spectrum up to a cutoff energy E_2 . Balancing the cooling and heating rates gives the resonant equilibrium Compton temperature T_c which, we shall see, is proportional to the energy of the first cyclotron harmonic,

$$E_B = 11.6 B_{12} \text{ keV}. \quad (5)$$

The constant of proportionality depends in detail on the energy and angular distribution of the incident photon flux, but the resonant Compton temperature reflects the characteristic energy of the resonant line, *not* the considerably larger characteristic energy of the photon continuum. This temperature is expected to be realized in the very outermost fringes of the scattering atmosphere, where line processes dominate the cooling and heating and $\tau_1 \ll 1$.

Cooling and heating rates due to magnetic continuum scattering are also easily calculated for $\tau_c \ll 1$. Balancing these rates gives the continuum equilibrium temperature. For $s \sim 1$ and $E_2 \sim 2m_e c^2$, this temperature is $\sim m_e c^2/4$, the same as its nonmagnetic counterpart. We expect this temperature to be approached at very large depths ($\tau_c \rightarrow 1$) inside the atmosphere where continuum cooling and heating dominates the corresponding line processes.

The intermediate optically thick regime in which $\tau_1 \gg 1$ but $\tau_c \ll 1$ cannot be treated analytically, and we investigate it numerically using a Monte Carlo radiative transfer code. We include the first three harmonics in our treatment of the line processes, and we study in detail the regime in which the cyclotron first harmonic is optically thick in the line core but thin in the wings. This regime is relevant for the line-forming regions of the γ -ray bursts GB 880205 and GB 870303, and possibly of many other bursts as well. Resonant scattering of higher harmonic photons contributes significantly to the energy balance when $\tau_2 \gtrsim 1$. Because excited Landau levels tend to decay by electric dipole emission, higher harmonic photons tend to “spawn” first harmonic photons whenever they are resonantly scattered. Thus, they affect the energy balance both directly, through their primary resonant scatters, and indirectly, in their subsequent manifestation as “spawned” photons. For isotropic power-law photon injection with $s \approx 1$, we find that the equilibrium Compton temperature due to *resonant* scattering is $\approx 0.27 E_B$ and is approximately *independent* of the column depth from $N_e \approx 10^{20}$ – $10^{22} \text{ electrons cm}^{-2}$, corresponding to $\tau_1 \approx (1-100) B_{12}^{-1}$ (see eq. [1]). Thus, the outer, cyclotron line-forming region in γ -ray bursts is naturally expected to be relatively cool.

Although we do not study the temperature dependence in nonisothermal layers in detail, it is clear that the *minimal* additional heating due to the continuum drives the equilibrium temperature above the pure line value, allowing us to speculate, at least crudely, about the expected temperature profile. The importance of the continuum in the atmospheric energy balance increases with column density and continuum spectral hardness (as measured by s and E_2 in our models). The thickness of the line-dominated region is naturally defined as the depth at which continuum heating causes a significant deviation of the actual equilibrium temperature (a factor of 2, say) from its pure line value. As we shall see, we estimate that the overall energy balance shifts from exclusively line heated and cooled to predominantly continuum heated and line cooled at a column depth $N_e \sim 10^{21}$ – $10^{22} \text{ electrons cm}^{-2}$.

In the dynamics portion of this paper, we calculate the line-enhanced radiation force analytically in the optically thin case ($\tau_c \ll \tau_1 \ll 1$) and numerically, by Monte Carlo methods, in the optically thick case ($\tau_c \ll 1 \ll \tau_1$). In the optically thin regime, this force is linearly proportional to the injected photon spectrum at E_B and to the column depth but is independent of the slab temperature. In the optically thick case, we shall see that the line-enhanced radiation force depends relatively weakly on column density ($\propto N_e^{0.4}$) and depends explicitly on the slab temperature as well. Assuming that cyclotron lines are produced in a gravitationally bound, ion-dominated layer near the surface of a neutron star, we can derive an upper bound on the distance to the line-forming region by requiring that the line-enhanced radiation force be insufficient to expel the scattering layer. From the resulting distance limit, we can, in turn, set an upper limit to the total luminosity of the γ -ray burst, the *magnetic* Eddington luminosity. In the optically thin case, the magnetic Eddington limit is ~ 0.01 times the ordinary (nonmagnetic) value and is independent of the field strength for $s = 1$. In the optically thick case, the magnetic Eddington limit for $s \approx 1$ is somewhat larger than the corresponding optically thin result, is moderately depth dependent ($\propto N_e^{0.6}$), and depends explicitly on the temperature and field strength in the slab.

In order to compare our results with observations, we have adopted the continuum spectral parameters of the burst GB 880205 in our optically thick studies. Our discussion of the scattering energetics and dynamics is otherwise quite general and our Monte Carlo calculations could easily be done for any input photon spectrum.

The spectra of GB 880205 and GB 870303 acquired by the Los Alamos/ISAS *Ginga* team display statistically significant harmonically separated absorption-like features at ≈ 20 and 40 keV (Murakami *et al.* 1988; Fenimore *et al.* 1988). These observations furnish the strongest evidence to date for cyclotron lines in γ -ray burst spectra. Taken together with the earlier more controversial claim that line features are present in $\sim 20\%$ of all γ -ray burst spectra (Mazets and Golenetskii 1981), these observations strongly suggest that many, if not all, γ -ray bursts originate from the environs of Galactic neutron stars.

The three outstanding characteristics of the lines observed by *Ginga* are (1) the comparable line strengths of the first ($E \approx 20$ keV) and second ($E \approx 40$ keV) harmonic line features, (2) the relative narrowness of the lines in spite of the hardness of the continuum emission, and (3) the absence of pronounced higher harmonic lines. A first harmonic feature centered at ≈ 20 keV indicates a field strength $B_{12} \sim 2$ (see eq. [5]). The narrowness of the lines suggests a cool line-forming region with $T \sim 5$ keV, while the absence of a third harmonic implies a relatively thin line-forming region with $N_e \lesssim 5 \times 10^{21}$ electrons cm^{-2} (see eq. [4]). Wang *et al.* (1989) and Lamb *et al.* (1989) argued that cyclotron resonant and Raman scattering in such a cool, moderately thin layer can explain the observed line strength hierarchy, provided that the characteristic optical depth of the second harmonic line $\tau_2 \sim 1$, which in turn implies $\tau_1 \gtrsim 10$ and $\tau_3 \lesssim 0.1$ (see eqs. [1], [3], [4]).

Wang *et al.* (1989) and Lamb *et al.* (1989) further proposed that the line-forming layer would naturally remain fairly cool if its temperature were dictated by the exact balance of heating and cooling due primarily to resonant cyclotron scattering, which gives $T \approx E_B/4 \approx 5$ keV. Using Monte Carlo methods, Wang *et al.* (1989) calculated emergent line spectra imposed on incident continua passing through such Compton-balanced layers. The incident photons were injected isotropically outward with a fixed, two-power-law continuum. The field strength B and temperature T were assumed to be constant throughout the layer of thickness N_e . Theoretical spectra were convolved with the relevant *Ginga* response functions, and the resulting theoretical counts spectra were compared directly with observations of GB 880205. From this analysis, Wang *et al.* (1989) found best-fit and 1σ confidence intervals $B_{12} = 1.71 \pm 0.07$ and $N_{e,21} = 1.2 \pm 0.6$ for this burst. The implied resonant Compton temperature $T_C = 5.3^{+0.3}_{-0.2}$ keV. The temperature in these models was fixed by the physical model, but the column depth was left as a free parameter. The range of acceptable column depths for the line-forming region implied by fits to the GB 880205 data is of the same order of magnitude as the thickness of the line-dominated region which we determined physically in the present study. This suggests that the line-dominated region plays an important, if not central, role in the line formation process.

Applying the distance constraint derived from the line-enhanced radiation force to GB 880205 gives $D \lesssim 200$ pc, implying a total hard X-ray ($\lesssim 1$ MeV) luminosity $L \lesssim 0.3$ times the nonmagnetic Eddington luminosity for an electron-proton plasma. This distance is consistent with the idea that GB 880205 originated from a neutron star in the galactic disk. In addition, at $D \lesssim 200$ pc, the number of photons received from GB 880205 is equivalent to the number that would be emitted by a blackbody at a temperature $\lesssim 0.3$ keV. This is consistent with the idea that Compton upscattering of a soft photon background by energetic electrons may be responsible for the production of γ -rays in this burst (and possibly also in GB 870303).

In § IIa we study the energetics of cyclotron resonant scattering and nonresonant continuum scattering analytically for optically thin lines. In § IIb, we study the scattering energetics numerically using Monte Carlo methods for optically thick lines. In § IIIa, we study the radiation force exerted on the scattering layer due to cyclotron resonant scattering and nonresonant continuum scattering analytically for optically thin lines. In § IIIb we study the line-enhanced radiation force numerically using Monte Carlo methods for optically thick lines. In this section, we also derive a distance constraint based on this radiation force. We argue that the distance to GB 880205 is $\lesssim 200$ pc and discuss the implications of this distance bound. We summarize our results in § IV.

II. SCATTERING ENERGETICS

a) *The Optically Thin Case*

i) *Resonant (Cyclotron) Cooling and Heating Rates*

We specialize here to the limit in which the slab is optically thin in the cyclotron first harmonic so that the single-scattering formalism applies. In this regime, equations (1)–(4) imply that we may neglect continuum scattering and scattering involving higher harmonic photons to an excellent approximation. Therefore, we restrict ourselves here to the cooling and heating rates resulting from resonant scattering of photons at the first cyclotron harmonic. Our derivation generalizes the method used by Rybicki and Lightman (1979, pp. 199–201) to compute the single-particle power from ordinary Compton scattering. We first calculate the single-particle power from resonant cyclotron scattering, which we then convolve with an electron momentum distribution—taken

to be a nonrelativistic Maxwellian—to compute the cooling and heating rates. Aside from properties of the incident photon spectrum, the only physical parameters in this problem are the cyclotron energy, E_B , and the electron temperature, T .

For our analytic calculations, we use the polarization-averaged classical magnetic Compton cross section with zero natural line width. In the longitudinal rest frame of the scattered electron, where the electron velocity along the magnetic field is zero before scattering, this cross section is given by

$$\frac{d\sigma}{d\Omega'_{sc}} = \frac{r_0^2}{2} \left[\sin^2 \theta' \sin^2 \theta'_{sc} + (q'_+ + q'_-) \left(\frac{1 + \mu'^2}{2} \right) \left(\frac{1 + \mu'^2_{sc}}{2} \right) \right]. \quad (6)$$

In this expression, $q'_\pm = 1/(1 \pm E_B/E')$, r_0 is the classical electron radius, (θ', θ'_{sc}) are, respectively, the incident and scattered angles of the photon relative to the magnetic field \mathbf{B} , $(\mu', \mu'_{sc}) = (\cos \theta', \cos \theta'_{sc})$, and all (primed) quantities are measured in the rest frame. In equation (6), there is one resonance at $E' = E_B$ which is described by the q'_- term; higher harmonic resonances, which we ignore, are absent in a classical treatment of the scattering. Since the resonance is very sharp (natural line width $\ll E_B$), we rewrite equation (6) in the following approximate form,

$$\frac{d\sigma}{d\Omega'_{sc}} \approx \frac{r_0^2}{2} \left[\sin^2 \theta' \sin^2 \theta'_{sc} + q'_+ \left(\frac{1 + \mu'^2}{2} \right) (1 + \mu'^2_{sc}) \right] + \frac{3}{4} \pi r_0 \delta(E' - E_r^0) \left(\frac{1 + \mu'^2}{2} \right) \left(\frac{1 + \mu'^2_{sc}}{2} \right), \quad (7)$$

where

$$E_r^0 = \frac{[1 + 2b(1 - \mu'^2)]^{1/2} - 1}{1 - \mu'^2} = \frac{2b}{[1 + 2b(1 - \mu'^2)]^{1/2} + 1} \quad (8)$$

is the rest frame resonant cyclotron absorption energy and $b = B/B_c$. The singularity at $\mu' = 1$ in the expression for E_r^0 is not physical as is evident from the latter expression for E_r^0 in equation (8). Throughout this paper, we use units for which $\hbar = c = k_B = 1$, where k_B is Boltzmann's constant. Equation (7) conveniently divides the continuum and resonant contributions to the cross section. Near the resonance, the δ -function dominates, while far from resonance both for $E' \ll E_B$ and $E' \gg E_B$, equation (7) assumes the correct limiting forms (see eq. [6]):

$$\begin{aligned} \frac{d\sigma}{d\Omega'_{sc}} &\rightarrow \frac{r_0^2}{2} \sin^2 \theta' \sin^2 \theta'_{sc}, & E' \ll E_B; \\ &\rightarrow \frac{r_0^2}{2} \left[\sin^2 \theta' \sin^2 \theta'_{sc} + \left(\frac{1 + \mu'^2}{2} \right) (1 + \mu'^2_{sc}) \right], & E' \gg E_B. \end{aligned} \quad (9)$$

The single-particle scattered power (in ergs s^{-1} per electron), P_{sc} , is a Lorentz scalar so that

$$P_{sc} = \left(\frac{dE}{dt} \right)_{sc} = \int d\Omega' \int dE' n_\gamma(E', \Omega') \int d\Omega'_{sc} E'_{sc} \frac{d\sigma}{d\Omega'_{sc}}, \quad (10)$$

where E'_{sc} is the scattered energy in the rest frame. The incident power, P_{inc} , is given by

$$P_{inc} = \left(\frac{dE}{dt} \right)_{inc} = \int d\Omega \int dE n_\gamma(E, \Omega) E \sigma_{lab}, \quad (11)$$

where $n_\gamma(E, \Omega) dE d\Omega$ is the photon density in the energy interval $(E, E + dE)$ and solid angle interval $(\Omega, \Omega + d\Omega)$, $d\sigma/d\Omega'_{sc}$ is the differential scattering cross section in the rest frame, and

$$\sigma_{lab} = (1 - \beta\mu) \sigma_{rest}, \quad \sigma_{rest} = \int d\Omega'_{sc} \frac{d\sigma}{d\Omega'_{sc}}. \quad (12)$$

For $d\sigma/d\Omega'_{sc}$, we use the resonant portion of equation (7), viz.,

$$\frac{d\sigma}{d\Omega'_{sc}} = \frac{3}{4} \pi r_0 \delta(E' - E_r^0) \frac{1}{2} (1 + \mu'^2) \frac{1}{2} (1 + \mu'^2_{sc}). \quad (13)$$

Using one-dimensional kinematics, we obtain

$$E'_{sc} = E' - E' \frac{E'}{2m_e} (\mu' - \mu'_{sc})^2 + O \left[E' \left(\frac{E'}{2m_e} \right)^2 \right]. \quad (14)$$

The first term on the right-hand side is only the one kept in the ‘‘Thomson limit,’’ in which electron recoil is ignored, and gives the leading order cooling of the electrons. The negative definite second term gives the leading order heating of the electrons due to recoil.

To evaluate P_{sc} , we invoke the Lorentz invariance of $n_\gamma(E, \Omega) dE d\Omega/E$, i.e.,

$$\frac{n_\gamma(E', \Omega') dE' d\Omega'}{E'} = \frac{n_\gamma(E, \Omega) dE d\Omega}{E}. \quad (15)$$

We assume that n_γ is a separable function of μ and E so that

$$n_\gamma(E, \Omega) = N(E) \frac{Q(\mu)}{2\pi}, \quad (16)$$

where $Q(\mu)$ gives the angular distribution of the photons and $\int_{-1}^{+1} d\mu Q(\mu) = 1$. We rewrite the δ -function in equation (13) in terms of laboratory frame quantities:

$$\delta(E' - E_r^0) = \frac{1}{\gamma(1 - \beta\mu)} \delta(E - E_i^0), \quad (17)$$

where

$$E_i^0 = \frac{E_r^0}{\gamma(1 - \beta\mu)}. \quad (18)$$

Substituting equations (13), (17), (14), (15), and (16) into equation (10) for P_{sc} and evaluating the integrals over energy and scattered angles gives

$$P_{sc} = \pi^2 r_0 \int_{-1}^{+1} d\mu Q(\mu) N(E_i^0) E_r^0 (1 + \mu'^2) \left[1 - \frac{E_r^0}{m_e} \left(\frac{\mu'^2}{2} + \frac{1}{5} \right) \right]. \quad (19)$$

To evaluate P_{inc} , we use equation (13) in equation (12), substitute the resulting σ_{lab} into equation (11), and evaluate the energy integral to get

$$P_{inc} = \pi^2 r_0 \int_{-1}^{+1} d\mu Q(\mu) N(E_i^0) E_r^0 (1 + \mu'^2) \frac{1}{\gamma^2(1 - \beta\mu)}. \quad (20)$$

Combining equations (19) and (20) gives the net single particle power from resonant cyclotron scattering:

$$P_S = P_{sc} - P_{inc} \approx \pi^2 r_0 \int_{-1}^{+1} d\mu Q(\mu) N(E_i^0) E_r^0 (1 + \mu'^2) \left[1 - \frac{1}{\gamma^2(1 - \beta\mu)} - \frac{E_r^0}{m_e} \left(\frac{\mu'^2}{2} + \frac{1}{5} \right) \right]. \quad (21)$$

The first two terms in brackets give the net (cooling) power in the zero recoil limit, while the third term gives the leading order recoil heating.

The electron velocity along the field is β , while its characteristic gyration velocity (orthogonal to the field) squared is of $O(b)$. These are the two small expansion parameters in equation (21). The leading order cooling is $O(\beta^2) \sim T/m_e$. Physically, an electron moving through the radiation field (photon gas) experiences a drag force, f_{drag} , due to its collisions with photons. In one-dimensional motion, this drag force to leading order is simply proportional to $-\beta$ which vanishes on average (over any electron velocity distribution that is even in β). The energy loss rate per electron (cooling) is then $-f_{drag}\beta \propto \beta^2$, which does not vanish on average since $\beta^2 \sim \beta_{th}^2 \equiv 2T/m_e$. In addition to the drag force, there is a velocity independent force (to lowest order in β) due to the radiation pressure (see eq. [78]). The work done by this force is simply proportional to β , which vanishes on average (for zero bulk flow velocity). The leading order heating comes from the term $O(b)$, which is just the recoil heating due to the fraction $\sim E/m_e \sim E_B/m_e = b$ of the incident photon energy given to an electron in a scattering event.

We expand the integrand in equation (21) to $O(\beta^2)$ and $O(b)$ to get

$$P_S = \pi^2 r_0 N(E_B) E_B \int_{-1}^{+1} d\mu Q(\mu) \left\{ -\beta\mu(1 + \mu^2) + \beta^2[1 + 2\mu^2 - 3\mu^4 - \alpha\mu^2(1 + \mu^2)] - b(1 + \mu^2) \left(\frac{\mu^2}{2} + \frac{1}{5} \right) + O(\beta^3, b\beta) \right\}, \quad (22)$$

where

$$\alpha \equiv \frac{E_B}{N(E_B)} \frac{dN}{dE} \Big|_{E=E_B}. \quad (23)$$

In arriving at equation (22), we have Taylor expanded $N(E_i^0)$ about E_B to linear order in β . Physically, this expansion means that only photons in the vicinity of the cyclotron first harmonic are allowed to engage in resonant scattering. This is a direct consequence of our assumption that the electrons are nonrelativistic; i.e., $\beta \sim \beta_{th} \ll 1$ (see eq. [18]). Indeed, from the resonance condition in equation (17), it is evident that given a photon arbitrarily far from the cyclotron first harmonic, there is always a sufficiently relativistic electron that can participate in resonant scattering. The frequency behavior of the resonant cross section is very sharp as measured in the electron rest frame, but it need not be so sharp as measured in the laboratory frame. For a nonrelativistic distribution of electrons, the laboratory frame does not deviate much from the rest frame. The first, second, and third terms in the braces in equation (22) give, respectively, the work done by the radiation force, the cooling due to the drag force, and the recoil heating.

The averaged net cooling rate (in $\text{ergs cm}^{-3} \text{s}^{-1}$) is given by

$$F = \Lambda_{line} - \Gamma_{line} = \int_{-\infty}^{+\infty} dp f(p) P_S(p), \quad (24)$$

where Λ_{line} is the average of the cooling terms in equation (22), Γ_{line} is the average of the recoil heating, and $p = \gamma\beta m_e$ is the momentum of the electron along the field. In our model, the distribution of electron momenta along the field, $f(p)$, is taken to be (quasi-)thermal. Although electron-photon scattering tends to accelerate electrons relative to ions, we assume that electrostatic coupling between electrons and protons (or other heavy ions) through collisional or collective processes suffices to maintain (quasi-)thermality (see § I). Thus, we take $f(p)$ to be a one-dimensional nonrelativistic Maxwellian,

$$f(p)dp = n_e \frac{e^{-u^2}}{\sqrt{\pi}} du, \quad (25)$$

where n_e is the electron density and $u = (p/m_e)/\beta_{\text{th}}$. We justify this nonrelativistic approximation (i.e., $T/m_e \ll 1$) *a posteriori* (see eq. [48], § IIb(ii)). From equations (22), (24), and (25) we obtain

$$\Lambda_{\text{line}} \approx n_e \pi^2 r_0 N(E_B) E_B \left(\frac{T}{m_e}\right) \int_{-1}^{+1} d\mu Q(\mu) [1 + 2\mu^2 - 3\mu^4 - \alpha\mu^2(1 + \mu^2)], \quad (26)$$

and

$$\Gamma_{\text{line}} \approx n_e \pi^2 r_0 N(E_B) E_B \int_{-1}^{+1} d\mu Q(\mu) \left[b(1 + \mu^2) \left(\frac{\mu^2}{2} + \frac{1}{5}\right) \right]. \quad (27)$$

Equations (26) and (27) depend only on the local spectral photon density n_γ at E_B . We assume that photons impinge on a scattering layer with an angular distribution $Q(\mu)$, and we relate n_γ (in photons $\text{cm}^{-3} \text{s}^{-1} \text{keV}^{-1}$) to $N_{\text{loc}}(E)$, the local photon flux density (in photons $\text{cm}^{-3} \text{keV}^{-1}$ in units where $c = 1$), by

$$n_\gamma(E, \Omega) = \frac{N_{\text{loc}}(E)}{2\pi} \frac{Q(\mu)}{\int_0^1 d\mu Q(\mu)\mu}. \quad (28)$$

For isotropic injection, $Q(\mu) = \Theta(\mu)$ (where $\Theta(\mu) = 1$ in $\mu \in [0, 1]$ and is zero otherwise), and

$$n_\gamma(E, \Omega) = \frac{N_{\text{loc}}(E)\Theta(\mu)}{\pi}, \quad (29)$$

so that

$$N(E) = 2N_{\text{loc}}(E). \quad (30)$$

Taking

$$N_{\text{loc}}(E) = A_{\text{loc}} \left(\frac{E}{E_b}\right)^{-s}, \quad (31)$$

and substituting equation (30) into (26) and (27) gives the leading order line cooling

$$\Lambda_{\text{line}} = \frac{16}{15} n_e \pi^2 r_0 A_{\text{loc}} \left(\frac{E_B}{E_b}\right)^{-s} (s+2) \left(\frac{T}{m_e}\right) E_B = \frac{16}{5} n_e \pi^2 r_0 A_{\text{loc}} E_b \left(\frac{T}{m_e}\right), \quad (32)$$

and the leading order line heating

$$\Gamma_{\text{line}} = \frac{32}{15} n_e \pi^2 r_0 A_{\text{loc}} E_b \left(\frac{E_b}{2m_e}\right) \left(\frac{E_B}{E_b}\right)^{2-s} = \frac{16}{15} n_e \pi^2 r_0 A_{\text{loc}} E_b b, \quad (33)$$

where the second expression in each equation is for $s = 1$.

ii) Nonresonant (Continuum) Cooling and Heating Rates

We now calculate the cooling rate, Λ_{cont} , and the heating rate, Γ_{cont} , due to magnetic continuum scattering in the limit $\tau_c \ll 1$.

This calculation closely parallels the derivation in § IIa(i) above. We start with equations (10)–(12) but now use the nonresonant portion of equation (7) for $d\sigma/d\Omega'_{\text{sc}}$, viz.,

$$\frac{d\sigma}{d\Omega'_{\text{sc}}} \approx \frac{r_0^2}{2} \left[\sin^2 \theta' \sin^2 \theta'_{\text{sc}} + q'_+ \left(\frac{1 + \mu'^2}{2}\right) (1 + \mu'^2_{\text{sc}}) \right]. \quad (34)$$

Working to leading order in the cooling and heating, i.e., to $O(\beta^2)$ and $O(E/2m_e)$, the averaged cooling rate is given by

$$\Lambda_{\text{cont}} = \frac{1}{2} n_e \sigma_T \left(\frac{T}{m_e}\right) \int d\mu Q(\mu) \int dE N(E) E \left\{ \sin^4 \theta + \frac{E^2}{(E + E_B)^2} \left[(1 + 4\mu^2 - \mu^4) + 2 \frac{E_B}{E + E_B} \mu^2 (1 + \mu^2) \right] \right\}, \quad (35)$$

and the averaged heating rate is given by

$$\Gamma_{\text{cont}} = \frac{1}{4} \frac{n_e \sigma_T}{m_e} \int d\mu Q(\mu) \int dE N(E) E^2 \left[\sin^4 \theta \left(\mu^2 + \frac{1}{5}\right) + \frac{E^2}{(E + E_B)^2} (1 + \mu^2) \left(\mu^2 + \frac{2}{5}\right) \right], \quad (36)$$

where $\sigma_T = 8\pi r_0^2/3$ is the Thompson cross section. Hereafter we specialize to isotropic injection into a forward hemisphere, i.e., $Q(\mu) = \Theta(\mu)$. We then have

$$\Lambda_{\text{cont}} = \frac{8}{15} n_e \sigma_T \left(\frac{T}{m_e}\right) \int_{E_1}^{E_2} dE E N_{\text{loc}}(E) \left[1 + \frac{4E^2}{(E + E_B)^2} + \frac{2E^2 E_B}{(E + E_B)^3} \right], \quad (37)$$

and

$$\Gamma_{\text{cont}} = \frac{2}{15} \frac{n_e \sigma_T}{m_e} \int_{E_1}^{E_2} dE E^2 N_{\text{loc}}(E) \left[1 + \frac{4E^2}{(E + E_B)^2} \right]. \quad (38)$$

Taking equation (31) for $N_{\text{loc}}(E)$, the energy integrals in equations (37) and (38) can be done analytically for integer s (see the Appendix). Here we take $s = 1$. This is approximately true, for instance, for the continuum spectrum of GB 880205 from 1 keV to 1 MeV. Assuming in addition that $E_2 \gg E_B \gg E_1$, we obtain

$$\Lambda_{\text{cont}} = \frac{16}{3} n_e \sigma_T A_{\text{loc}} E_b \left(\frac{T}{m_e}\right) \left(\frac{E_2}{2m_e}\right) m_e, \quad (39)$$

and

$$\Gamma_{\text{cont}} = \frac{4}{3} n_e \sigma_T A_{\text{loc}} E_b \left(\frac{E_2}{2m_e}\right)^2 m_e. \quad (40)$$

In the classical nonrelativistic treatment presented here, equations (39) and (40) are strictly valid for $T/m_e \ll 1$ and $E_2/2m_e \ll 1$. The expressions (39) and (40) are the same as their nonmagnetic counterparts. The expressions for Λ_{cont} and Γ_{cont} for general indices s in the limit $E_2 \gg E_B \gg E_1$ are given in the Appendix.

iii) Resonant and Nonresonant Cooling and Heating Time Scales

The resonant cooling and heating time scales are

$$t_{\text{line}}^{\text{cool}} \equiv \frac{E_e}{\Lambda_{\text{line}}}, \quad (41)$$

and

$$t_{\text{line}}^{\text{heat}} \equiv \frac{E_e}{\Gamma_{\text{line}}}, \quad (42)$$

where $E_e \sim T$ is the characteristic electron energy. The continuum cooling and heating time scales are defined as in equations (41) and (42), but with $\Lambda_{\text{line}} \rightarrow \Lambda_{\text{cont}}$ and $\Gamma_{\text{line}} \rightarrow \Gamma_{\text{cont}}$. From equations (39) and (40), we have

$$\frac{t_{\text{line}}^{\text{cool}}}{t_{\text{cont}}^{\text{cool}}} = \frac{\Lambda_{\text{cont}}}{\Lambda_{\text{line}}} = \frac{40}{9\pi} e^2 \left(\frac{E_2}{2m_e}\right) \approx 10^{-2} \left(\frac{E_2}{2m_e}\right), \quad (43)$$

and from equations (40) and (33), we have

$$\frac{t_{\text{line}}^{\text{heat}}}{t_{\text{cont}}^{\text{heat}}} = \frac{\Gamma_{\text{cont}}}{\Gamma_{\text{line}}} = \frac{10}{3\pi} e^2 \left(\frac{E_2}{2m_e}\right)^2 b^{-1} \approx 8 \times 10^{-3} \left(\frac{E_2}{2m_e}\right)^2 b^{-1}, \quad (44)$$

where e^2 is the fine-structure constant. From equations (43) and (44), it is evident that for $b \gtrsim 10^{-2}$ line heating and cooling dominate over continuum heating and cooling, even for $E_2/2m_e = 1$. For softer incident spectra, with either a smaller high-energy cutoff ($E_2 \ll 2m_e$) or a steeper power-law index ($s > 1$), the line dominance is even more pronounced.

In the very early phases of heating a cold ($T \approx 0$) electron gas, Λ_{cont} and Λ_{line} are both negligible and the relative strength of the line and continuum heating is given by equation (44). The line heating thus dominates when $b(E_2/2m_e)^{-2} \gg 8 \times 10^{-3}$, even though the bandwidth for the resonance approaches zero (more accurately, it approaches the natural line width) as $T \rightarrow 0$. This is because in the optically thin limit the heating depends on the *oscillator strength* of the resonance, not just on the bandwidth. Thus, $\Gamma \sim n_e A_{\text{loc}} E_b \times (\text{oscillator strength}) \times (\text{fractional energy transferred per scatter})$, which gives $\Gamma_{\text{line}} \sim n_e A_{\text{loc}} E_b \pi r_0 b$ and $\Gamma_{\text{cont}} \sim n_e A_{\text{loc}} E_b \sigma_T E_2 (E_2/2m_e)$, where $\sigma_T E_2$ is the ‘‘oscillator strength’’ for continuum scattering.

If the radiation source is a neutron star that emits isotropically from a patch on the surface, the local flux and the observed flux are related by

$$N_{\text{loc}} = N_{\text{obs}} \frac{D^2}{R^2} f_p^{-1}, \quad (45)$$

where R is the neutron star radius, D is the distance to the star, and the parameter f_p depends in general on the covering fraction, f_a , of the patch, on the orientation of the patch relative to the observer, and the angular distribution of injected photons from the patch. If the injection is isotropic and $f_a = 1$ (whole surface radiating), $f_p = 1$. If the injection is isotropic and $f_a \ll 1$ (radiating hot spot), $f_p \approx 2f_a$. Taking $E_e \sim T$ in equation (41) and using equation (32) with $s = 1$ and equation (45) gives

$$t_{\text{line}}^{\text{cool}} \approx (3 \times 10^{-9} \text{ s}) \left(\frac{R_{10}}{D_{100}}\right)^2 \left(\frac{A_{\text{obs}} E_b}{8.1}\right)^{-1} f_p, \quad (46)$$

where $R = 10R_{10}$ km and $D = 100D_{100}$ pc. The flux $A_{\text{obs}} E_b$ is normalized to that for GB 880205 between 1 keV and 1 MeV. Similarly, equation (42) gives

$$t_{\text{line}}^{\text{heat}} \approx (5 \times 10^{-9} \text{ s}) \left(\frac{T}{5 \text{ keV}} \right) B_{12}^{-1} \left(\frac{R_{10}}{D_{100}} \right)^2 \left(\frac{A_{\text{obs}} E_b}{8.1} \right)^{-1} f_P. \quad (47)$$

As we shall see later, $T_C \sim 5$ keV in the scattering layer, so equation (47) is a good estimate of the time for the layer to reach the equilibrium Compton temperature.

iv) *The Resonant and Nonresonant Compton Temperatures*

Substituting equations (22) and (25) into equation (24) for the net cooling rate, F , and setting $F = 0$ gives the equilibrium resonant Compton temperature

$$T_C = \frac{I_1}{I_2} E_B [1 + O(b)], \quad (48)$$

where

$$I_1 = \int_{-1}^{+1} d\mu Q(\mu) (1 + \mu^2) \left(\frac{\mu^2}{2} + \frac{1}{5} \right), \quad (49)$$

$$I_2 = \int_{-1}^{+1} d\mu Q(\mu) [1 + 2\mu^2 - 3\mu^4 - \alpha\mu^2(1 + \mu^2)].$$

The properties of the injected photon spectrum are embodied in I_1 and I_2 .

We evaluate the leading order T_C for various $Q(\mu)$. We assume $N(E) \propto E^{-s}$ so that $\alpha = -s$.

Case 1: $Q(\mu) = \Theta(\mu)$; photons are injected isotropically in $\mu \in [0, 1]$:

$$T_C = \frac{E_B}{2 + s}. \quad (50)$$

Case 2: $Q(\mu) = \frac{1}{2}$. This corresponds to a fully isotropic photon distribution. The expression for T_C is the same as in equation (50).

Case 3: $Q(\mu) = \delta(\mu \pm 1)$. Photons are beamed parallel (−) or antiparallel (+) to the field:

$$T_C = \frac{7}{10} \frac{E_B}{s}. \quad (51)$$

Case 4: $Q(\mu) = \delta(\mu)$. Photons are beamed orthogonal the field:

$$T_C = \frac{E_B}{5}. \quad (52)$$

Case 5: $Q(\mu) = \Theta(\mu - \mu_0)/(1 - \mu_0)$. Photons are isotropically injected in $\mu \in [\mu_0, 1]$:

$$T_C = \frac{E_B}{2 + s} \left[1 - \frac{3}{8} \mu_0 \left(1 + \frac{7}{6} \mu_0^2 + \frac{1}{2} \mu_0^4 \right) \right] / \left[1 - \frac{15}{8(2 + s)} \mu_0 \left(1 + \frac{2 + s}{3} \mu_0^2 + \frac{s - 3}{5} \mu_0^4 \right) \right]. \quad (53)$$

Equation (53) reduces to equation (50) when $\mu_0 = 0$ and when $\mu_0 \rightarrow -1$, and to equation (51) when $\mu_0 \rightarrow 1$, as it must.

It is evident from equations (50)–(53) that with the exception of injection orthogonal to the field (eq. [52]), the Compton temperature T_C is undefined for certain power-law indices. A simple explanation for this behavior follows from considering the (resonant) radiation drag force. The temperature T_C results from a balance of the kinematic cooling described by the first two terms in brackets in equation (21) against the recoil heating described by the third term. For beamed injection along the field ($\mu = 1$), the kinematic cooling can be written *exactly* as $-f\beta$, where

$$f = 2\pi^2 r_0 E_B N \left[\frac{E_B}{\gamma(1 - \beta)} \right] = 2\pi^2 r_0 E_B \left[N(E_B) + \beta E_B \frac{dN}{dE} \Big|_{E_B} + \dots \right] \quad (54)$$

is the force on the electron. This force depends on β only through the photon density N . For a flat spectrum, f is *manifestly* velocity independent, and the kinematic cooling vanishes on average. The Compton temperature in this case diverges, in agreement with equation (51). If $dN/dE|_{E_B} < 0$ (corresponding to $s > 0$ for a power law), the drag force in equation (54) is $\propto -\beta$ which gives an averaged positive kinematic cooling. This gives a well-defined T_C . If $dN/dE|_{E_B} > 0$ (corresponding to $s < 0$), the drag force is $\propto +\beta$ giving an averaged kinematic cooling that is *negative* (heating), resulting in an undefined T_C . Alternatively, from the resonance condition (see eq. [17], [18], [8]) and the scattering kinematics in the zero recoil limit (see eq. [14]), the scattered photon energy is given in terms of the photon energy by

$$\frac{E_{\text{sc}} - E_{\text{inc}}}{E_{\text{inc}}} = (1 - \mu_{\text{sc}}) \left(\frac{E_B - E_{\text{inc}}}{E_B} \right) + O \left[\left(\frac{E_B - E_{\text{inc}}}{E_B} \right)^2 \right]. \quad (55)$$

Thus, photons redward of E_B contribute to kinematic *cooling*, while those blueward of E_B contribute to kinematic *heating*. If $dN/dE|_{E_B} < 0$, low-energy photons ($E < E_B$) dominate and kinematic cooling results, while if $dN/dE|_{E_B} > 0$, high-energy photons ($E > E_B$) dominate and kinematic heating results.

A similar argument can be made for isotropic injection, for which the drag force is easily seen to vanish when $s + 2 = 0$. In this case, however, a simple “thermodynamic” argument can also be used to derive the Compton temperature, equation (50). In the absence of stimulated processes, the photon field will tend to equilibrate to a Wien distribution function, $N(E)/E^2 \propto f(E) = \exp(-E/T)$, at the electron temperature T . Thus, for isotropic injection, the net resonant heating/cooling should be proportional to $\{T d \ln [N(E)/E^2] / d \ln E + E\}|_{E_B}$, or $-T(s + 2) + E_B$ for $N(E) \propto E^{-s}$. The net heating/cooling vanishes when $T = T_C = E_B/(s + 2)$ for isotropic injection.

For injection involving intermediate ranges of μ , it is natural to expect critical values of s intermediate between those for beamed $\mu = 1$ injection and for isotropic injection. Thus, equation (53) spans the range between equations (50) and (51), to which it tends in the appropriate limits. Beam injection orthogonal to the field ($\mu = 0$) is a somewhat special case, because the drag force is independent of $dN/dE|_{E_B}$, as is evident from equation (22). Therefore, T_C is independent of s in this case. (Note in this case that the component of the radiation pressure force along the field is zero, as expected.) The resonant scattering nature of the electron-photon interaction is central to these constraints on values of s for which T_C has sensible (finite and positive) values. Consequently, analogous restrictions do *not* arise for continuum scattering, magnetic or otherwise.

We have compared the analytic results for T_C in equations (50)–(53) with the numerical Monte Carlo results. For the beamed injection models, we used $B_{12} = 1.66$ and a line-of-sight optical depth at the cyclotron first harmonic of ≈ 0.01 to ensure single scattering. The Monte Carlo results agree with the analytical results in equations (51) and (52) to within $\sim 5\%$.

For isotropic injection with $\mu \in [0, 1]$, we used $B_{12} = 1.71$ and an optical depth along the field (parallel to slab normal) of ≈ 0.03 and 0.3. In both cases, T_C (Monte Carlo) ≈ 4.7 keV, while equation (50) predicts 7.0 keV. The discrepancy arises because, in a plane-parallel slab, the limit of $\tau_1 \ll 1$ for all μ is *never* attained. This is because the optical depth along any given ray with direction cosine μ to the field is τ_1/μ , which can never be much less than unity for all μ . Thus, in our test runs with $\tau_1 = 0.03$ along the field, the region of μ -space with $\mu < 0.03$ has an optical depth greater than unity. The multiple scatterings resulting from the $\sim 3\%$ of photons injected into this “pathological” region enhances the cooling, resulting in a T_C lower than predicted from the single-scattering limit. Indeed, for $\tau_1 = 0.001$, so that only $\sim 0.1\%$ of photons are injected with a line-of-sight optical depth greater than unity, we obtain agreement between the Monte Carlo and analytic results to within $\sim 5\%$. Alternatively, we injected photons with $\mu \in [0.1, 1]$. Using $\tau_1 = 0.03$ along the field [so that $0.03 < \tau_1$ (line of sight) < 0.3] and $B_{12} = 1.71$, we find better than 5% agreement between the Monte Carlo results and the analytic result of 7.2 keV predicted from equation (53).

Balancing the continuum cooling and heating rates, equations (39) and (40), gives the equilibrium Compton temperature resulting from magnetic continuum scattering alone,

$$T_C^{\text{cont}} = \frac{1}{4} \left(\frac{E_2}{2m_e} \right) m_e \quad (56)$$

for $s = 1$, precisely the same as for nonmagnetic Thompson scattering. This agreement does not hold for all s , but the difference is at most in logarithmic factors (see the Appendix).

b) The Optically Thick Regime

Using a Monte Carlo code, we now turn to the cooling and heating arising from resonant cyclotron and nonresonant magnetic continuum scattering in media that are optically thick in the core of the cyclotron first harmonic but thin in the line wings; i.e.,

$$1 \ll \tau_1 \ll 1/a, \quad (57)$$

where

$$a = \frac{\Gamma_{\text{rad}}}{2E_B(2T/m_e)^{1/2}} = 1.8 \times 10^{-3} B_{12} \left(\frac{T}{\text{keV}} \right)^{-1/2} \quad (58)$$

is the dimensionless natural line width (see Wang, Wasserman, and Salpeter 1988). At these depths, the continuum is always optically thin.

In our simulations, we take the magnetic field to be parallel to the slab normal and adopt a power-law incident photon continuum of the form:

$$N_{\text{loc}}(E) = A_{\text{loc}}(E/E_b)^{-s}, \quad \begin{aligned} s &= 0.846 \text{ for } 1 \text{ keV} \leq E \leq E_b, \\ s &= 1.174 \text{ for } E_b \leq E \leq 1000 \text{ keV}, \end{aligned} \quad (59)$$

and $E_b = 101.3$ keV, where the parameters are determined from a fit to the GB 880205 spectrum outside its two cyclotron features (Wang *et al.* 1989). Photons enter the scattering layer isotropically distributed in the outward half-plane, that is, with an angular distribution $Q(\mu) = \Theta(\mu)$.

The code includes the first three cyclotron harmonics, employing polarization-averaged resonant scattering cross sections with finite natural line width derived using quantum mechanics in the weak field ($b \ll 1$) limit (see Wang and Lamb 1989). We treat “photon spawning,” which arises from scattering involving higher harmonic ($n > 1$) photons, fully, and incorporate relativistic kinematics in all aspects of the scattering process. In our code, we use classical, polarization-averaged cross sections for magnetic continuum scattering (see eq. [34].) We follow the life history of each photon scatter-by-scatter and simply sum the energy and dynamical quantities for a particular simulation. Details of the code will be given elsewhere (see Wang *et al.* 1990).

The underlying assumptions made in constructing our Monte Carlo code should be valid for GB 880205 and GB 870303, and perhaps for other γ -ray bursts as well. The weak field approximation is appropriate for both GB 880205 and GB 870303, whose cyclotron features imply $b \approx 0.04 \ll 1$. Polarization averaging is a fairly good approximation at low electron densities n_e (electrons cm^{-3}) $\ll 10^{22} B_{12}^4$ (see Gnedin, Pavlov, and Shibano 1978; Wang, Wasserman, and Salpeter 1988). For GB 880205, where the column density has been well-determined by Wang *et al.* (1989), n_e (electrons cm^{-3}) $\sim 10^{20}/l_{10}$, where $l(\text{cm}) = 10l_{10}$ is the thickness of the line-forming region. [For comparison, the scale height of an isothermal layer in hydrostatic balance near the surface of a neutron star of mass $1.4 M_\odot$ and radius 10 km would be $\approx 10T$ (keV) cm.]

By simulating the transfer of a large number of photons ($\gtrsim 10^5$), we can calculate the average net cooling within the slab due to electron-photon scattering fairly accurately. In order to isolate the resonant, cyclotron line cooling and heating, we only follow photons injected between 1 and 100 keV, which should suffice to completely include the resonant effects of the first three cyclotron harmonics. For all of the cooling calculations discussed in this section (and also for the momentum deposition calculations discussed below) we adopt the field strength $B_{12} = 1.71$, the field strength that gives the best fit to the line spectrum of GB 880205. However, to compute the equilibrium Compton temperature, T_C/B_{12} , due primarily to resonant scattering (i.e., the bottom curve in Fig. 5), we employ a set of field strengths between $B_{12} = 1.5$ and 2.1.

i) Cyclotron Line Cooling and Heating

We define the net cooling due to resonant scattering in the line-forming region to be K_{net} . In Figure 1, we plot the *net specific cooling*, $C \equiv K_{\text{net}}/N_{\text{loc}}(E_B)E_B$, in keV per photon due to cyclotron resonant scattering as a function of N_e for $T = 8, 10.7$, and 16 keV. These temperatures correspond to 1.5, 2.0, and 3.0 times $T_C = 5.35$ keV, which is the resonant Compton temperature for $B_{12} = 1.71$ and $N_{e,21} = 1.2$, the best-fit parameters for the line spectrum of GB 880205. Superposed on this plot is the net cooling found when photon spawning is ignored, i.e., the net cooling due solely to resonant scattering of photons at the cyclotron first harmonic (*filled symbols*). The 1σ Monte Carlo statistical errors for all the data in this figure are about the size of the symbols representing the data points and are not shown. Evidently, at large N_e , where $\tau_2 \gtrsim 1$, spawning increases the net cooling substantially (e.g., by a factor ~ 2 at $N_{e,21} = 12$; see § IIb[ii]).

The net cooling K_{net} is the difference between the cooling K and heating due to line processes. Qualitatively, we may understand the Monte Carlo results in the following way. We may write the cooling K as

$$K = f_s N_{\text{loc}}(E_B) \Delta E_w \Delta E_c, \quad (60)$$

where f_s is the fraction of line photons that scattered, $N_{\text{loc}}(E_B)$ is the line flux density in photons $\text{cm}^{-2} \text{s}^{-1} \text{keV}^{-1}$, ΔE_w is the effective line width in keV, and ΔE_c is the characteristic energy transferred to a photon that interacted. When $1 \ll \tau_1 \ll 1/a$, $f_s \sim 1$ for all photons within $\Delta E_w \approx E_B(2T/m_e)^{1/2}(\ln \tau_1)^{1/2}$ of E_B . For the photons in this range, $\Delta E_c \sim \Delta E_w$. Assuming these photons to be the main contributors to K , we therefore obtain the rough estimate

$$K \sim N_{\text{loc}}(E_B) E_B \left[E_B \frac{T}{m_e} \ln(1 + \tau_1) \right], \quad (61)$$

where we introduce the argument $1 + \tau_1$ in the logarithm to ensure that $K \rightarrow 0$ when $\tau_1 \rightarrow 0$. When $T \gg T_C$, cooling dominates heating so that $K_{\text{net}} \rightarrow K$. When $T \rightarrow T_C$, $K_{\text{net}} \rightarrow 0$. Combining these two facts together with equation (61), we construct the following *Ansatz* for the general expression for K_{net} :

$$K_{\text{net}} \sim N_{\text{loc}}(E_B) E_B \left[E_B \frac{T - T_C}{m_e} \ln(1 + \tau_1) \right]. \quad (62)$$

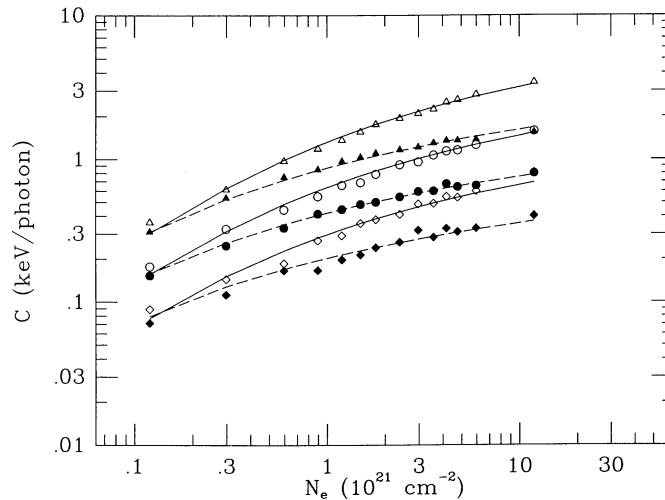


FIG. 1.—The net specific line cooling (keV per photon), C , as a function of N_e for $T = 8$ (diamond), 10.7 (circle), and 16 keV (triangle). These temperatures correspond to 1.5, 2.0, and 3.0 times $T_C = 5.35$ keV, the resonant Compton temperature at $B_{12} = 1.71$ and $N_{e,21} = 1.2$, the best-fit parameters to the line spectrum of GB 880205. The filled symbols represent the cooling due solely to resonant scattering at the cyclotron first harmonic. The fitting curve is given by eq. (63), represented by the dashed line. The open symbols represent cooling including the first three harmonics and photon spawning. The fitting curve is given by eq. (64), represented by the solid line. The 1σ Monte Carlo statistical errors for all the data in this figure are about the size of the symbols representing the data points and are not shown.

This *Ansatz* suggests we plot C against the “natural” variable $E_B[(T - T_C)/m_e] \ln(1 + \tau_1)$ when displaying the variation of the net cooling with N_e and T for all $\tau_1 \ll 1/a$, and this is done in Figure 2 (using the data in Fig. 1). The fits in Figure 1 are based on equation (62). For the data that ignore spawning (*filled symbols*), the fit is

$$C = 0.84E_B \frac{T - 5.98(\text{keV})}{m_e} \ln(1 + 0.89\tau_1), \quad (63)$$

where $T_C = 5.98$ keV is a fitted parameter. The fit to the data is better than 20%. For the data that include spawning (*open symbols*), the fit is given by

$$C = 1.23E_B \frac{T - T_C(\text{keV})}{m_e} \left(1 + 1.50 \frac{T - T_C}{T + T_C}\right) \ln(1 + 0.23\tau_1), \quad (64)$$

where $T_C = 5.27$ keV is derived from the best-fit constant to the bottom curve in Figure 5 (see § IIb[ii] below). This fit to the data is better than 25%; dispensing with the correction factor to our “*Ansatz*” worsens the fit somewhat.

When $T < T_C$, there is net *heating*. In Figure 3a we superpose the plot of net heating versus N_e for $T = 3.6$ keV $= 2/3T_C$ with the plot for net cooling versus N_e for $T = 8$ keV $= 3/2T_C$. In Figure 3b, we repeat this for $T = 1/2T_C$ and $2T_C$. It is evident that the heating plateaus at large N_e more strongly than the cooling. We plot in Figure 4 the net specific cooling C as a function of temperature for $N_{e,21} = 0.12, 0.30, 1.2, 3.6, 12$. Two features are evident from this plot. First, for temperatures not too far from T_C , the net cooling/heating is roughly symmetric in T about T_C . Second, in all cases, there are zero crossings at $T \approx 5$ keV. This equilibrium Compton temperature, T_C , varies only weakly across two orders of magnitude in N_e .

ii) The Resonant Compton Temperature T_C

From our Monte Carlo code, we have computed the equilibrium Compton temperature, T_C , that results from cyclotron resonant scattering. For this purpose, we only followed photons injected between 1 and 100 keV to ensure that the resulting T_C is due primarily to cyclotron resonant scattering. We have computed T_C for a variety of models with $0.12 \leq N_{e,21} \leq 12$ and $1.50 \leq B_{12} \leq 2.10$. This range of column depths and field strengths includes the range of acceptable fits of the model of Wang *et al.* (1989) to the GB 880205 spectrum. In their model, it was assumed that line heating and cooling dominate the thermal balance of the line-forming region. The temperature of the scattering layer (T_C) was therefore determined by following photons injected between 1 and 100 keV, and was not a free parameter but rather was determined by $N_{e,21}$ and B_{12} . The numerical results for T_C/B_{12} determined in this manner are shown as a function of N_e in the lower curve (*circular data points*) in Figure 5. Remarkably, $T_C/B_{12} \approx 3.08$ keV (*equivalently*, $T_C \approx 0.27E_B$) for all models in this range. This constancy corroborates the results of Figure 4. The horizontal bars beneath the best-fit constant line at $T_C/B_{12} = 3.08$ denote the 1, 2, and 3 σ confidence intervals in N_e derived from fitting the self-consistent temperature models of Wang *et al.* (1989) to a line spectrum of GB 880205.

At higher column depths ($N_{e,21} \gtrsim 6$), the Compton temperature tends to decrease from the flat plateau at lower N_e 's. At such depths, the second harmonic becomes optically thick, and the optical depth at the third harmonic approaches unity (see eq. [1]–[4]). Consequently, essentially all second harmonic photons and many third harmonic photons resonantly scatter and spawn photons

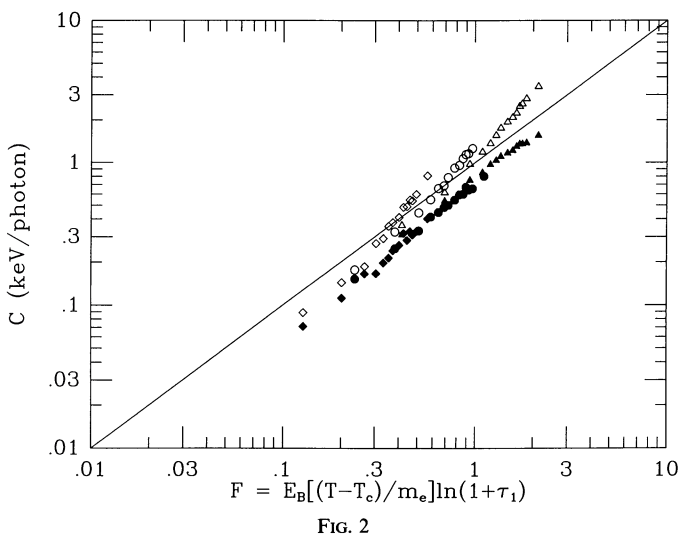


FIG. 2

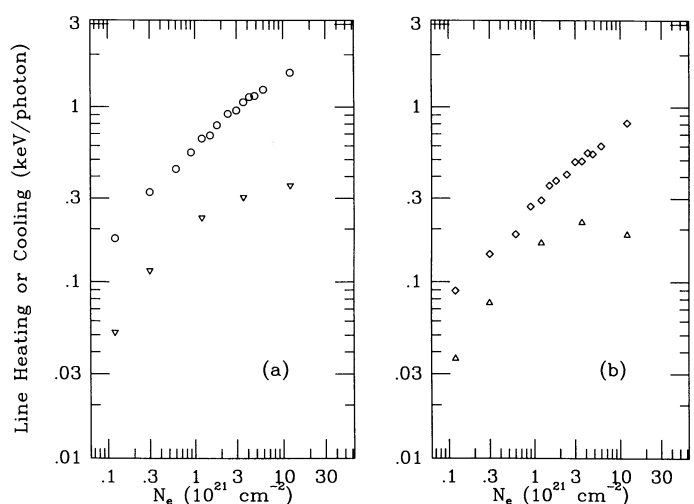


FIG. 3

FIG. 2.—The net specific line cooling data of Fig. 1 plotted as a function of the “natural” variable, $\mathcal{F} \equiv E_B[(T - T_C)/m_e] \ln(1 + \tau_1)$, with $T_C = 5.35$ keV and τ_1 given by eq. (1). The solid line corresponds to $C = \mathcal{F}$. The symbols have the same meaning as in Fig. 1. The deviations from $C = \mathcal{F}$ seen in the data with the open symbols is due to the higher harmonic transitions and the associated photon spawning.

FIG. 3.—(a) The net specific line heating vs. N_e for $T = 2.7$ keV ($= T_C/2$, $T_C = 5.35$ keV) (*inverted triangle*) superposed on the net specific line cooling vs. N_e for $T = 10.7$ keV ($= 2T_C$) (*circle*). (b) Same as (a), but for $T = 3.6$ keV ($= 2T_C/3$) (*triangle*) and $T = 8$ keV ($= 3T_C/2$) (*diamond*). $B_{12} = 1.71$ for all the data. The 1 σ Monte Carlo statistical errors are about the size of the symbols representing the data points and are not shown.

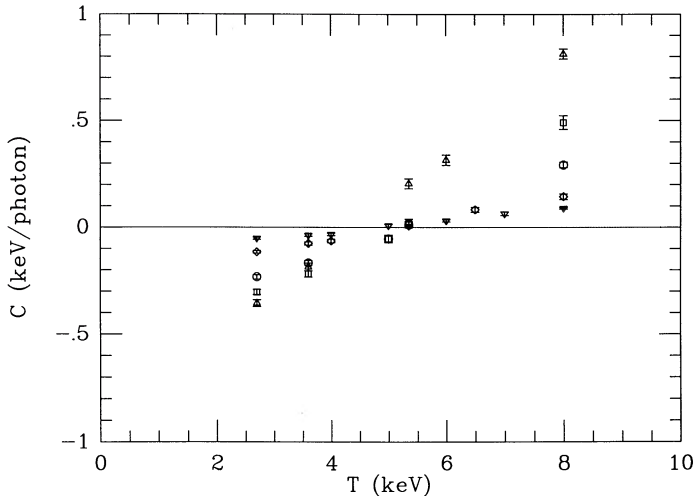


FIG. 4

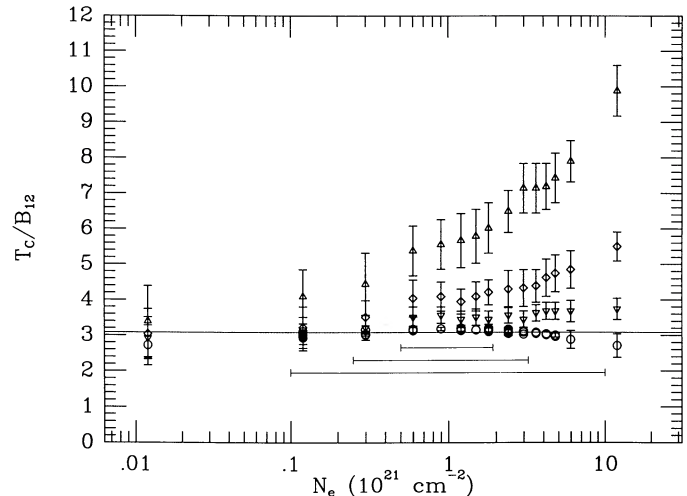


FIG. 5

FIG. 4.—The net specific line cooling as a function of temperature for $N_{e,21} = 0.12$ (inverted triangle), 0.30 (diamond), 1.2 (circle), 3.6 (box), and 12 (triangle). $B_{12} = 1.71$ for all the data. The error bars are 1σ Monte Carlo statistical errors. Note the zero crossings at ≈ 5 keV across the two orders of magnitude in N_e shown.

FIG. 5.—The Compton temperature, T_C , in units of B_{12} , as a function of N_e for injection spectra given by eq. (59) with an upper cutoff at $E_2 = 100$ (circle), 300 (inverted triangle), 511 (diamond), and 1000 keV (triangle). The Compton temperature with $E_2 = 100$ keV is due primarily to resonant scattering at the first three cyclotron harmonics (see Fig. 4). The horizontal line at $T_C/B_{12} = 3.08$ is the best-fit constant to these data at $N_{e,21} > 0.1$ ($\tau_1 > 1$). The influence of continuum heating becomes more pronounced with higher E_2 . The error bars are 3σ statistical errors derived from the Monte Carlo statistical errors in the cooling and heating data. The horizontal bars depict the 1, 2, and 3σ confidence intervals in N_e derived from fits of self-consistent temperature models (i.e., models with T_C/B_{12} fixed by pure line processes) to a line spectrum of GB 880205 (Wang *et al.* 1989).

near the first harmonic. Because of the anharmonic separation of the Landau levels ($E_N < NE_B$), spawning mainly produces first harmonic photons redward of line center. Resonant scattering of these “red” photons tends to cool the electrons. Spawning thus enhances the line cooling efficiency relative to the no spawning limit, thereby resulting in a lower value of T_C .

iii) Influence of the Continuum on T_C and the Thickness of the Line-dominated Layer

Wang *et al.* (1989) considered line formation models involving isothermal slabs with temperatures determined by line scattering processes only. Implicit in their treatment was the assumption that the continuum above 100 keV contributed negligibly to the thermal balance in the line-forming region. In this section, we investigate the effects of the high-energy continuum qualitatively and quantitatively and estimate the column density range in which the Wang *et al.* assumptions are valid. Although, strictly speaking, we would need radiative transfer calculations for *nonisothermal* scattering layers to do this problem justice, we shall nevertheless offer plausible conjectures for the full atmospheric structure using results gleaned from our isothermal simulations.

In our model calculations, we assume that the scattering layer where the lines form lies above the region where the continuum is formed. While it seems necessary for the X-ray ($\lesssim 100$ keV) portion of the continuum spectrum to be formed below the scattering layer, this may not be the case for the γ -ray continuum (> 100 keV). We do not consider here the formation of the continuum (but see § IIIb[ii]). Rather we inject a given continuum into the scattering layer and investigate qualitatively, analytically and numerically, the consequent temperature structure in this layer. The scattering layer where the lines form is optically thin in the continuum. The continuum heating is therefore linearly proportional to N_e . (The continuum cooling is unimportant compared to the continuum heating at $T \ll m_e$.) At low column depths, this continuum heating is negligible and line processes dominate, giving rise to a temperature $T = T_C \sim E_B$ (see eq. [48] and the lower curve in Fig. 5). At very large depths, the continuum ultimately dominates the line processes, giving rise to a temperature $\sim m_e$ (see eq. [56]). In the intermediate region where the temperature is less than $\sim m_e$, continuum heating and line cooling are in rough balance, which elevates the Compton temperature above the pure line value. It is difficult to make definite statements about this region from our single-zone calculations. Nevertheless, our basic picture of line and continuum cooling and heating can be used to make qualitative estimates of the actual temperature structure of this intermediate zone. We show in Figure 6 a schematic depiction of the temperature structure in this scattering layer.

At low densities, photon scattering (as described in the preceding sections) will dominate cooling and heating. In general, the energy balance equation for the atmosphere is

$$H_{\text{cont}} + H_{\text{line}} = K_{\text{cont}} + K_{\text{line}}, \quad (65)$$

where H_i is the heating rate (in $\text{ergs cm}^{-2} \text{s}^{-1}$) and K_i is the cooling rate for process i . The continuum optical depth is much less than unity throughout the regions we discuss, i.e., $N_{e,21} \ll 1400$ (see eq. [2]). We may therefore always use the optically thin results for H_{cont} and K_{cont} , i.e., equations (35) and (36) with $n_e \rightarrow N_e$. For rough, order-of-magnitude estimates of the line heating and cooling, we ignore higher harmonic transitions and consider only the cyclotron first harmonic. For simplicity, we assume a $1/E$ incident photon spectrum injected isotropically into the scattering atmosphere.

At very low depths, $\tau_1 \ll 1$, or from equation (1),

$$N_{e,21} \ll 0.01 B_{12} \left(\frac{T}{\text{keV}} \right)^{1/2}. \quad (66)$$

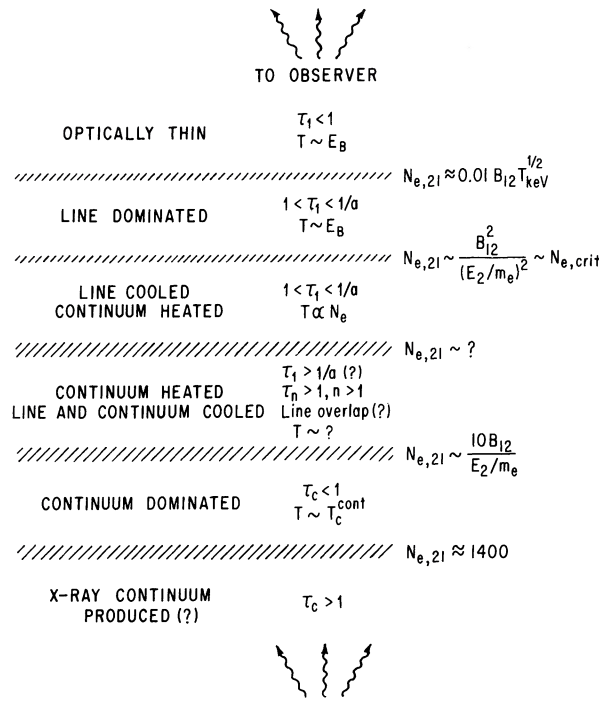


FIG. 6.—Schematic depiction of the temperature structure in the scattering layer

Line processes dominate here (see eq. [43], [44]), and the equilibrium temperature is proportional to E_B (see eqs. [32], [33]), independent of N_e . Inclusion of the continuum heating would raise the equilibrium temperature only slightly and would not alter the N_e dependence.

At larger depths where $1 \ll \tau_1 \ll 1/a$, or from equation (58),

$$0.01 B_{12} \left(\frac{T}{\text{keV}} \right)^{1/2} \ll N_{e,21} \ll 6 \left(\frac{T}{\text{keV}} \right), \tag{67}$$

the continuum heating is unimportant at first but becomes increasingly significant as N_e increases. For the line processes, we estimate the cooling as

$$K_{\text{line}} \sim A_{\text{loc}} E_b E_B \frac{T}{m_e} \ln \tau_1 \propto BT \ln \tau_1 \tag{68}$$

(see eq. [62]) and the heating as

$$H_{\text{line}} \sim A_{\text{loc}} E_b E_B \frac{B}{B_c} \ln \tau_1 \propto B^2 \ln \tau_1 \tag{69}$$

(see eq. [62]). As long as line processes dominate, the equilibrium temperature is the line-dominated value of T_c discussed above, and the temperature does not vary significantly with depth. The situation changes when continuum heating becomes larger than line heating. From equations (40) (with $n_e \rightarrow N_e$) and (69), we find that $H_{\text{cont}} > H_{\text{line}}$ when

$$N_{e,21} > N_{e,crit} \sim 3B_{12}^2 \left(\frac{E_2}{2m_e} \right)^{-2} \left(\frac{\ln \tau_1}{\ln 100} \right), \tag{70}$$

where we have chosen $\tau_1 = 100$ as a fiducial value in this region. When $N_{e,21} < N_{e,crit}$, the line processes dominate. When $N_{e,21} > N_{e,crit}$, so that $H_{\text{line}} < H_{\text{cont}}$, the balance of *continuum* heating and *line* cooling gives

$$T \sim \left[0.01 \left(\frac{E_2}{2m_e} \right)^2 B_{12}^{-1} N_{e,21} \left(\frac{\ln \tau_1}{\ln 100} \right)^{-1} \right] m_e, \tag{71}$$

which, using equation (70), can be written as

$$T \sim 15 B_{12} \left(\frac{N_{e,21}}{N_{e,crit}} \right) \text{keV}. \tag{72}$$

Thus, for $N_{e,21} < N_{e,crit}$, the equilibrium temperature is approximately independent of N_e , while for $N_{e,21} > N_{e,crit}$, the temperature

risers approximately linearly with N_e . This thickness of the line-dominated layer is given by $N_{e,\text{crit}}$. As is evident from equation (70), this thickness *decreases* as the hardness of the input spectrum (as parameterized by E_2) *increases*.

The linear rise of T with N_e may be altered when continuum cooling becomes important compared to line cooling. Exactly where this transition occurs is hard to estimate because at large depths the line cooling may be modified significantly from equation (68) by increasingly significant contributions from higher harmonics, line overlap, and optical depth of the line wings. For a rough estimate, however, we use equation (68) for K_{line} . Combining this with equation (39) (with $n_e \rightarrow N_e$), $K_{\text{cont}} > K_{\text{line}}$ when

$$\frac{N_{e,21}}{N_{e,\text{crit}}} \gtrsim 10B_{12}^{-1} \left(\frac{E_2}{2m_e} \right), \quad (73)$$

which is much less than the Thomson depth. At greater depths, the continuum cooling and heating dominate the line processes, and we can write the energy balance in this region as

$$H_{\text{cont}} = K_{\text{cont}} + \epsilon, \quad (74)$$

where $\epsilon = K_{\text{line}} - H_{\text{line}}$ is the small but finite perturbation due to the net line cooling. The temperature in this region is expected to approach a constant (independent of N_e) that is generally less than that given by equation (56) due to the residual line cooling, but tends to equation (56) with increasing depth.

In the previous section, we computed T_C under the assumption that only line heating and cooling is significant. That assumption was implemented by restricting ourselves to injected photon energies less than $E_2 = 100$ keV. In this section we extend our calculations to include continuum heating and cooling in an isothermal “one-zone” atmosphere with column depth N_e , using our Monte Carlo code. To do so, we inject photons with the spectrum given by equation (59) and include the continuum heating for photons injected up to $E_2 = 300, 511,$ and 1000 keV for comparison. We investigate a sequence of slabs with column depths that satisfy equation (67). At much higher column depths, our treatment of the line radiative transfer becomes invalid.

In Figure 5 we plot the equilibrium Compton temperature (actually T_C/B_{12}) as a function of N_e from this sequence of “one-zone” models. As expected, the additional heating caused by the continuum forces the Compton temperature to rise above the value derived solely from line processes (recall that the cooling is proportional to T). From Figure 5, we estimate the thickness of the cool (~ 5 keV at $B_{12} \sim 2$) line-dominated layer to be the thickness where the continuum heating causes the temperature to deviate significantly from its pure line value. This critical column depth depends on the hardness of the injected spectrum, being smaller for a harder spectrum, but is generally $\sim (0.1-10) \times 10^{21} \text{ cm}^{-2}$ (for the curves with $E_2 > 100$ keV), in qualitative agreement with the expression for $N_{e,\text{crit}}$ in equation (70). Beyond $\sim N_{e,\text{crit}}$, the temperature begins to rise more steeply (e.g., see data point at $N_{e,21} = 12$ for $E_2 = 1000$ keV), again in qualitative agreement with the above discussion (see eq. [72], and the following discussion). Because our code employs the *classical* magnetic continuum cross section, which asymptotes to the Thompson scattering cross section instead of the smaller Klein-Nishina cross section at photon energies $E \gtrsim m_e$, we tend to *overestimate* continuum heating at high energies. As a result, we tend to overestimate T_C at $E_2 \gtrsim m_e$ particularly at relatively large column depths ($N_{e,21} \gtrsim N_{e,\text{crit}}$). Moreover, our code does not include $n \geq 4$ harmonics, which increase the line cooling and tends to lower T_C . Both these approximations lead us to *overestimate* T_C , and, hence, to *underestimate* the thickness of the line-dominated layer. However, even for $E_2 \gtrsim m_e$, we believe that our results for the value of the line-dominated layer thickness remains correct, at least in order of magnitude.

In their fits to the lines in a spectrum of GB 880205, Wang *et al.* (1989) assumed perfect heating and cooling balance due to *resonant* cyclotron scattering in the line-forming region, so that the temperature of this region was determined physically by pure line processes and was *not* an independently adjustable fitting parameter. Their fits indicate that the line-forming region is very thin, $\sim (0.1-10) \times 10^{21} \text{ cm}^{-2}$, which agrees in order of magnitude with the thickness of the line-dominated layer estimated above, both numerically and analytically (see $N_{e,\text{crit}}$ in eq. [70] with $E_2/2m_e \sim 1$; note that T_C for $E_2 = 1000$ keV in Figure 5 is probably higher than the actual value). This qualitative coincidence between the thickness of the line-dominated layer and the thickness of the line-forming layer strongly suggests that the line-dominated layer plays an important, if not central, role in the line formation process. To ascertain rigorously the connection (if any) between these two regions requires one to follow the spectral evolution through a multizone atmosphere whose temperature structure is determined from physical processes such as electron-photon scattering. Such studies are currently under way.

III. SCATTERING DYNAMICS

Radiation impinging on the scattering layer deposits momentum as well as energy. The energy deposition gives the cooling and heating balance discussed in § II. The momentum deposition gives the radiation force on the scattering layer (Mitrofanov and Palov 1982). In our model, the magnetic field is oriented parallel to the normal to the plane-parallel slab. Photons strike this layer from one side, which for concreteness, we take as the bottom side. We are interested in the component of the radiation force parallel to the magnetic field (=slab normal) along which the electrons move classically. Thus, we are interested in the force acting on the one-dimensional electron gas. (Protons, if present, are dragged along due to the strong electrostatic coupling with the electrons.)

a) The Optically Thin Case

i) The Resonant and Nonresonant Radiation Force

The radiation force is given by

$$\frac{\delta p}{\delta t} = \int sE \int d\Omega n_e(E, \Omega) \int d\Omega_{\text{sc}} \frac{d\sigma}{d\Omega_{\text{sc}}} \delta p, \quad (75)$$

with δp the momentum change of the electron along the field per scattering. The corresponding force per unit area acting in the direction of the slab normal is

$$P_{\text{RAD}} = \frac{\delta p}{\delta t} N_e, \quad (76)$$

where N_e is the column density of electrons through the slab (in cm^{-2}).

We work to zeroth order in v and $E/2m_e$. Assuming $v \ll 1$ and $E/2m_e \ll 1$,

$$\delta p \approx (\mu - \mu_{\text{sc}})E. \quad (77)$$

To calculate the resonant line force, we use equation (13) for $d\sigma/d\Omega_{\text{sc}}$ (dropping the primes and letting $E_r^0 = E_B$) and equation (77) with $E \rightarrow E_B$. Using equation (16) gives

$$\left(\frac{\delta p}{\delta t}\right)_{\text{line}} = \pi^2 r_0 N(E_B) E_B \int_{-1}^{+1} d\mu Q(\mu) \mu (1 + \mu^2). \quad (78)$$

Using equations (16), (28), and (31) gives

$$\left(\frac{\delta p}{\delta t}\right)_{\text{line}} = \pi^2 r_0 A_{\text{loc}} E_b \left(\frac{E_B}{E_b}\right)^{1-s} \mathcal{J}, \quad (79)$$

where

$$\mathcal{J} = \frac{\int_0^1 d\mu Q(\mu) \mu (1 + \mu^2)}{\int_0^1 d\mu Q(\mu) \mu}. \quad (80)$$

The corresponding radiation pressure force is

$$P_{\text{RAD}}^{\text{line}} = \frac{3}{4} \mathcal{J} \left[A_{\text{loc}} E_b \left(\frac{E_B}{E_b}\right)^{1-s} E_B \right] \left(\frac{2T}{m_e}\right)^{1/2} \tau_1, \quad (81)$$

where we have used equation (1). The expression in brackets is $N_{\text{loc}}(E_B) E_B^2$, the photon energy flux density at $E = E_B$. If the scattering layer is bound to the surface of a neutron star by gravity, we may obtain a limit on $N_{\text{loc}}(E_B) E_B^2$ by requiring that this line radiation force not exceed the force of gravity. The gravitational binding force per unit area is given by

$$P_{\text{grav}} = \frac{GM y}{R^2}, \quad (82)$$

where M is the neutron star mass, R is the neutron star radius, and we assume an e -ion plasma for the scattering layer by taking $y = \mu_e m_p N_e$, where μ_e is the mean molecular weight per electron for the plasma ($\mu_e = 1$ for an e - p plasma; see Shapiro and Teukolsky 1983, pp. 25–26). Requiring $P_{\text{RAD}}^{\text{line}} < P_{\text{grav}}$ gives a distance upper bound to the line radiation source. Taking D to be the distance to the source, using $s = 1$ in equation (81), and using equation (45), we obtain

$$D(\tau_1 \ll 1) < 38 M_{1.4}^{1/2} \left(\frac{A_{\text{obs}} E_b}{8.1}\right)^{-1/2} \mu_e^{1/2} f_p^{1/2} \mathcal{J}^{-1/2} \text{ pc}, \quad (83)$$

where $M_{1.4} \equiv M/1.4 M_\odot$, and where for specificity, we have normalized $A_{\text{obs}} E_b$ to that for GB 880205 between 1 keV and 1 MeV. (The optically thick bound relevant to GB 880205 is computed in § IIIb[ii].) For isotropic injection in the forward hemisphere ($Q[\mu] = \Theta[\mu]$), $\mathcal{J} = 3/2$, while for beam injection along the field ($Q[\mu] = \delta[\mu - 1]$), $\mathcal{J} = 2$. If f_p is comparable for these two modes of injection, then the distance bound is only weakly dependent on the injection angular distribution, varying by a factor of order unity between these two extreme modes of injection. From the distance bound, we infer the corresponding luminosity bound. Thus, using equation (83), assuming a $1/E$ spectrum for $N_{\text{loc}}(E)$ with $E_2 \gg E_1$, we have

$$L(\tau_1 \ll 1) \leq 4\pi R^2 F_E^{\text{loc}} = 4\pi R^2 \int_{E_1}^{E_2} dE E N_{\text{loc}}(E) < \left[8 \times 10^{-3} \left(\frac{E_2}{2m_e}\right) \right] L_E, \quad (84)$$

where

$$L_E = \frac{4\pi G M m_p c}{\sigma_T} = 1.77 \times 10^{38} \text{ ergs } M_{1.4} \text{ s}^{-1} \quad (85)$$

is the nonmagnetic Eddington luminosity. The right-hand side of equation (84) is the *magnetic* Eddington luminosity for a $1/E$ spectrum in the optically thin limit. As with its nonmagnetic counterpart, this Eddington limit is independent of the scattering layer thickness. However, since it is derived fundamentally from a physical limit on the spectral flux $N(E_B)$ at E_B , the magnetic Eddington luminosity depends on the shape of the continuum spectrum.

The calculation of the radiation force due to magnetic continuum scattering parallels the derivation of equation (78) except we use

equation (34) for $d\sigma/d\Omega_{\text{sc}}$ (dropping the primes):

$$\left(\frac{\delta p}{\delta t}\right)_{\text{cont}} = \frac{\sigma_T}{2} \int_{E_1}^{E_2} dE E N(E) \int_{-1}^{+1} d\mu Q(\mu) \mu \left[\sin^2 \theta + \frac{E^2}{(E + E_B)^2} (1 + \mu^2) \right]. \quad (86)$$

Taking $Q(\mu) = \Theta(\mu)$ and using equation (30) gives

$$\left(\frac{\delta p}{\delta t}\right)_{\text{cont}} = \frac{\sigma_T}{4} \int_{E_1}^{E_2} dE E N_{\text{loc}}(E) \left[1 + \frac{3E^2}{(E + E_B)^2} \right]. \quad (87)$$

Taking equation (31) for $N_{\text{loc}}(E)$, the integral in equation (87) can be done analytically for integer s (see the Appendix). Specializing to $s = 1$ and assuming $E_2 \gg E_B \gg E_1$, we have

$$\left(\frac{\delta p}{\delta t}\right)_{\text{cont}} \approx \sigma_T A_{\text{loc}} E_b E_2. \quad (88)$$

This expression is the same as for nonmagnetic Thomson scattering. This is not true for all power-law indices s , but the difference is at most in logarithmic factors (see the Appendix). (In the nonmagnetic case, eq. [88] gives the force along the z -direction for radiation injected isotropically into the xy -plane. The forces in the x and y directions average to zero.)

ii) Acceleration Time Scales

We assume in our model that the scattering layer is bound by gravity. If, however, the resonant line radiation force on this layer is the dominant force, the time to accelerate this layer to relativistic speeds, assuming an e - p plasma, is

$$t_{\text{line}}^{\text{accel}} = \frac{\gamma m_p}{(\delta p / \delta t)_{\text{line}}} \approx 2 \times 10^{-5} \gamma \left(\frac{R_{10}}{D_{100}} \right)^2 \text{ s}, \quad (89)$$

where γ is the Lorentz factor of the electrons and protons and where we have used equations (79) and (45), have taken $f_p = s = 1$, and have normalized $A_{\text{obs}} E_b$ to that for GB 880205. For an e^+e^- plasma, this acceleration time is reduced by $\sim m_p/m_e$ to $\sim 10^{-8}$ s.

For comparison, the continuum acceleration time scale is given by

$$\frac{t_{\text{cont}}^{\text{accel}}}{t_{\text{line}}^{\text{accel}}} = \frac{(\delta p / \delta t)_{\text{line}}}{(\delta p / \delta t)_{\text{cont}}} \approx 130 \left(\frac{E_2}{2m_e} \right)^{-1}, \quad (90)$$

where we have used equations (79) and (88) (see eqs. [43] and [44]).

b) The Optically Thick Case

i) The Radiation Force

Let $F_N^{\text{loc}}(E_1, E_2)$ be the photon number flux (in photons $\text{cm}^{-2} \text{s}^{-1}$) between energies E_1 and E_2 impinging (isotropically) on the slab and λE_B be the mean momentum deposited along the field in this layer (to the electrons) per photon. (Recall that we use $\hbar = c = 1$ so that $E_B/c \rightarrow E_B$.) The radiation force per unit area acting on the slab (along the slab normal) is then given by

$$P_{\text{RAD}} = F_N^{\text{loc}} \lambda E_B. \quad (91)$$

The function λ is determined numerically by directly averaging the momentum deposited by individual incident photons in the course of being either transmitted through or reflected from the scattering slab. The flux $F_N^{\text{loc}} = \int_{E_1}^{E_2} dE N_{\text{loc}}(E)$, with $N_{\text{loc}}(E)$ the photon number flux density. Taking equation (31) for $N_{\text{loc}}(E)$, we rewrite equation (91) as

$$\frac{P_{\text{RAD}}}{P_0} = \eta, \quad (92)$$

with

$$P_0 \equiv A_{\text{loc}} \left(\frac{E_B}{E_b} \right)^{-s} E_B^2 = N_{\text{loc}}(E_B) E_B^2 \quad (93)$$

and

$$\eta \equiv \left(\frac{E_B}{E_b} \right)^{s-1} \lambda \int_{x_1}^{x_2} dx x^{-s}, \quad (94)$$

where $x_2 \equiv E_2/E_b$ and $x_1 \equiv E_1/E_b$. The quantity P_0 is the radiation pressure force arising from the line photons at the cyclotron first harmonic in an E^{-s} spectrum if the effective line width were E_B . All of the physics of the momentum deposition resulting from the radiative transport of line and continuum photons are contained in η .

In each panel of Figure 7, we plot for given T , the dimensionless radiation pressure force η as a function of N_e for $E_2 = 100, 300, 511, \text{ and } 1000 \text{ keV}$. Without exception, we use $B_{12} = 1.71$ and $E_1 = 1 \text{ keV}$ in these simulations. The 1σ Monte Carlo statistical errors are about the size of the symbols representing the data points and are not shown. For $N_{\text{loc}}(E)$ we use equation (59). The filled

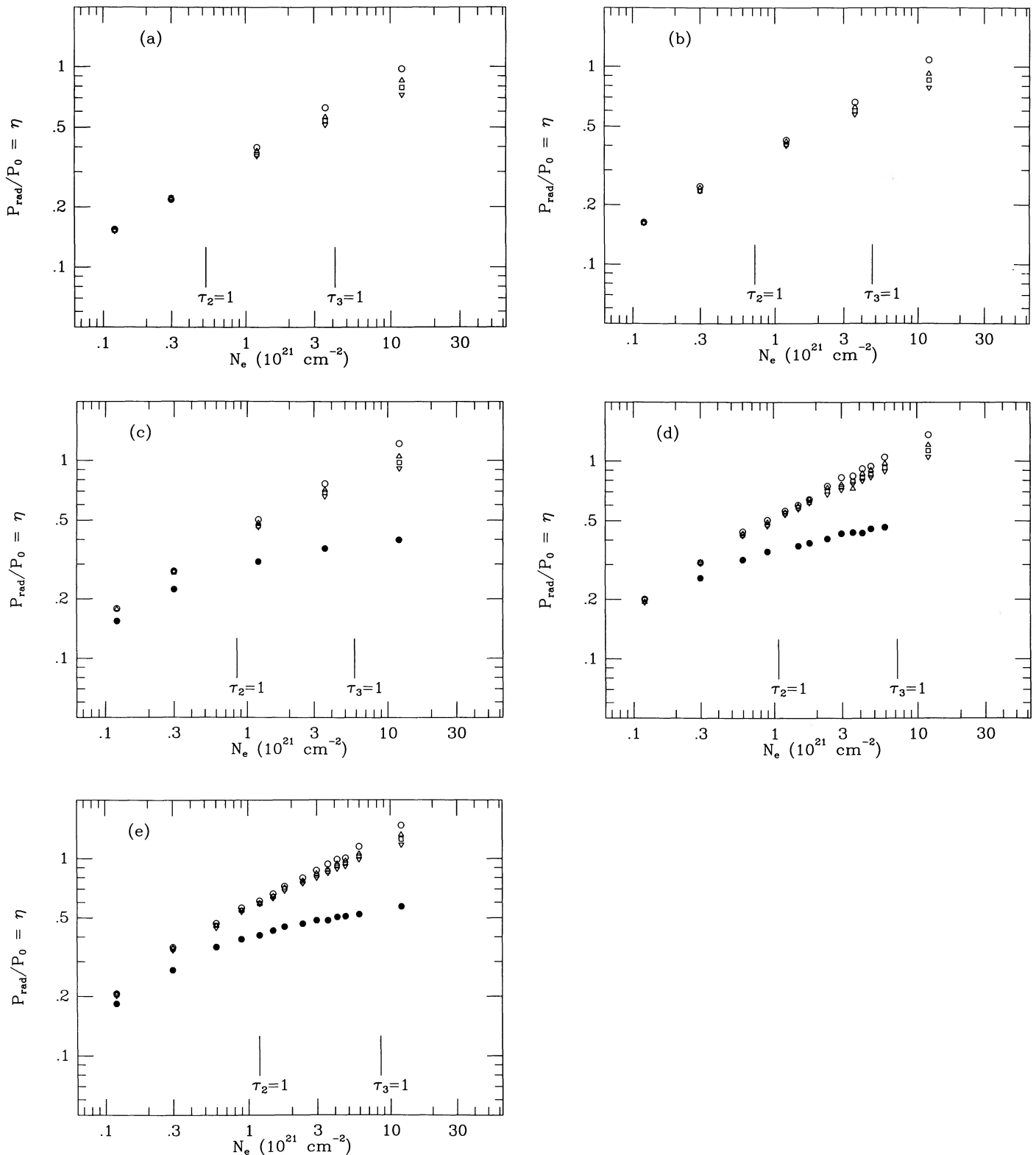


FIG. 7.—The dimensionless radiation pressure force, η , as a function of N_e for $T = (a)$ 2.7, (b) 3.6, (c) 5.35 ($= T_C$), (d) 8, (e) 10.7, and (f) 16 keV. The injection spectrum used is given by eq. (59) with an upper cutoff of $E_2 = 100$ (inverted triangle), 300 (box), 511 (triangle), and 1000 keV (circle). $B_{12} = 1.71$ for all the data. The 1σ Monte Carlo statistical errors are about the size of the symbols representing the data points and are not shown. The radiation pressure force with $E_2 = 100$ keV is due primarily to resonant scattering at the first three cyclotron harmonics. The filled symbols in (c)–(f) represent the radiation pressure force due solely to resonant scattering at the cyclotron first harmonic (= fundamental) i.e., higher harmonic transitions and the associated photon spawning are ignored. The vertical bars denote where the optical depth is unity in the second and third harmonics (see eq. [3], [4]). In (f), the location where the optical depth is unity for the first harmonic is also depicted (see eq. [1]).

symbols in Figures 7c–7f correspond to the case in which the radiation pressure arises solely from resonant scattering of photons at the first harmonic, with all higher harmonic transitions (and hence photon spawning) ignored. It is evident from Figures 7c–7f that the higher harmonic transitions contribute very substantially to the momentum deposition, especially at large N_e 's. These transitions contribute in two ways: the actual scattering of the higher harmonic photons that (usually) spawns photons *and* the spawning itself which produces photons (mostly) near the cyclotron first harmonic.

When $E_2 = 100$ keV, the radiation pressure η is mainly due to the line photons (in the range of N_e shown). We therefore take $\eta(E_2 = 100$ keV) as the radiation pressure due to the lines. As expected, the continuum contribution increases with E_2 , especially at large N_e 's. It is nevertheless remarkable that the effect of neglecting the continuum is far less serious than ignoring harmonic transitions. For example, at $N_{e,21} = 12$, $\eta(E_2 = 100$ keV)/ $\eta(0 \rightarrow 1 \rightarrow 0) = 2.3$, while $\eta(E_2 = 1000$ keV)/ $\eta(E_2 = 100$ keV) = 1.3. It is also evident from Figure 7 that although $\eta(0 \rightarrow 1 \rightarrow 0)$ starts to saturate at larger N_e 's where $\tau_1 \gg 1$, the curves including the higher harmonics and/or continuum keep on rising. The rise may be attributed to two distinct causes. First, the continuum radiation force rises linearly with N_e . Second, and more importantly, the higher harmonic forces are always *effectively optically thin*, in that at $B \ll B_c$ higher harmonic photons tend to undergo only a single resonant scatter before being degraded into multiple first harmonic photons. When $\tau_1 \lesssim 1$, the first harmonic always dominates, but for $\tau_1 \gg 1$, its contribution to the radiation pressure ultimately levels off. However, as N_e increases, the second harmonic becomes important, and then higher harmonics (see Fig. 7). Ultimately, at sufficiently large depths such that $\tau_{\text{cont}} \gtrsim 1$, continuum scattering dominates the radiation pressure.

To construct fitting formulae for the line force, we begin with a qualitative discussion analogous to our discussion of the line cooling above. Consider first the contribution to the momentum deposition due to resonant scattering at the cyclotron first harmonic, i.e., ignoring higher harmonic transitions. In Figure 8, we plot the resulting radiation pressure η as a function of N_e for $T = 5.35, 8, 10.7,$ and 16 keV ($T_C = 5.35$ keV). In analogous fashion to the description of the energy deposition, we write the momentum deposition (radiation pressure) as

$$P_{\text{RAD}} = f_s N_{\text{loc}}(E_B) \Delta E_w \Delta p_c, \quad (95)$$

where f_s is the fraction of line photons that scattered, $N_{\text{loc}}(E_B)$ is the line flux density in photons $\text{cm}^{-2} \text{s}^{-1} \text{keV}^{-1}$, ΔE_w is the effective line width in keV, and Δp_c is the characteristic momentum transferred (in keV) to the electrons per photon that interacted. When $\tau_1 \ll 1$, $f_s \sim \tau_1$, $\Delta E_w \sim$ the thermal Doppler width $= E_B(2T/m_e)^{1/2}$, and we recover the optically thin result within factors of order unity (see eq. [81]).

When $\tau_1 \gg 1$, $f_s \sim 1$ for photons within $\Delta E_w \approx E_B(2T/m_e)^{1/2}(\ln \tau_1)^{1/2}$ of E_B . Photons deep in the core suffer many scatters before escaping the medium either by reflection (emerging from the bottom of the slab) or by transmission (emerging from the top). Those that escape by reflection always push on the slab, while those that escape by transmission may either push or “pull” on the slab. Photons in the outer fringes of the core (and in the wings) suffer a single or at most a few scatters before escaping the medium. These photons give a net push to the slab (as in the optically thin limit). There are therefore three populations that contribute to Δp_c : A, the transmitted population that experienced multiple scattering; B, the reflected population that experienced multiple scattering; C, the “fringe” population that experienced at most a few scatters. To zeroth order, we assume that the push and pull contributions from the population A photons roughly cancel. The mean momentum transfer for a population B photon is $\sim E_B$ since it turns around with only a modest fractional energy change. The mean momentum transfer for photons in population C is also $\sim E_B$. It is reasonable to assume that populations B and C occupy a significant fraction of the photons that interacted, i.e., of f_s in equation (95). With this assumption, we have for the $\tau_1 \gg 1$ limit,

$$P_{\text{RAD}} \sim N_{\text{loc}}(E_B) E_B^2 \left[\left(\frac{2T}{m_e} \right)^{1/2} (\ln \tau_1)^{1/2} \right]. \quad (96)$$

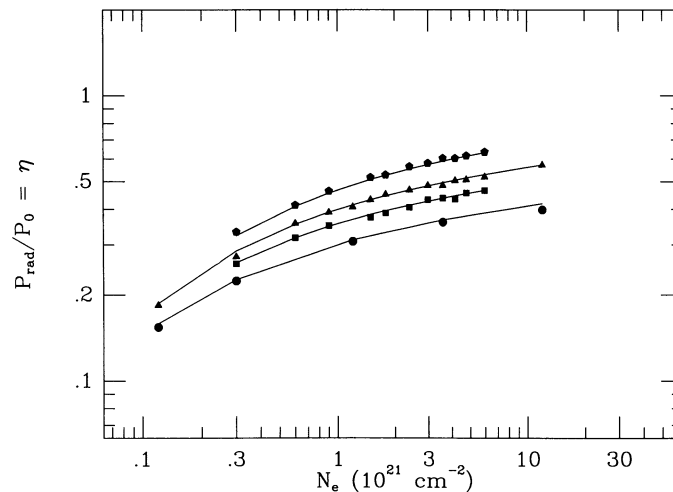


FIG. 8.—The dimensionless line radiation pressure force due solely to resonant scattering at the cyclotron first harmonic (higher harmonic transitions ignored) as a function of N_e for $T = 5.35$ ($= T_C$, circle), 8 (box), 10.7 (triangle), and 16 keV (pentagon). $B_{12} = 1.71$ for all the data. The 1σ Monte Carlo statistical errors are about the size of the symbols representing the data points and are not shown. The solid curves are given by the fitting formula in eq. (97).

A function for P_{RAD} that approaches the correct $\tau_1 \ll 1$ (eq. [81]) and $\tau_1 \gg 1$ (eq. [96]) limits and which fits the data very well is

$$\frac{P_{\text{RAD}}}{P_0} = \eta = 1.8 \left(\frac{T}{m_e} \right)^{1/2} \left[\ln \left(1 + \frac{0.32\tau_1^2}{1 + 0.55\tau_1} \right) \right]^{1/2}. \quad (97)$$

This function is plotted in Figure 8 for $T = 5.35, 8, 10.7,$ and 16 keV. The fit is good to better than $\sim 5\%$ for all the data shown.

Next, let us consider the contribution of the higher harmonics to the momentum deposition. In Figure 9, we plot for $E_2 = 100$ keV the radiation pressure η including the first three harmonics. The discussion of the physics of the contribution from the first harmonic is unaltered. For the contribution from the higher harmonics, we focus our discussion on the second harmonic. This discussion applies in general to all the higher harmonics.

When $\tau_2 \ll 1$, equation (81) still holds with $\tau_1 \rightarrow \tau_2$ and $E_B \rightarrow 2E_B$. When $\tau_2 \gg 1$, $f_s \sim 1$ in equation (95) for the photons within $\Delta E_w \sim 2E_B(2T/m_e)^{1/2}(\ln \tau_2)^{1/2}$ of $2E_B$. Because $B/B_c \ll 1$, the single scattering approximation still applies when $\tau_2 \gg 1$. Consequently, $\Delta p_c \sim 2E_B$. For $\tau_2 \gg 1$ we then have

$$P_{\text{RAD}}^{(n=2)} \sim N_{\text{loc}}(2E_B)(2E_B)^2 \left(\frac{2T}{m_e} \right)^{1/2} (\ln \tau_2)^{1/2} \quad (98)$$

for the direct contribution of $n = 2$ single scatters. A function with the same form as equation (97) can be used for $P_{\text{RAD}}^{(n=2)}$. In addition to the direct contribution to the momentum transfer from the single scattering, there is also an indirect contribution arising from the (mostly) cyclotron first harmonic photons that are usually spawned from the higher harmonic single-scatter event. Since the amount of spawning is proportional to τ_2 at $\tau_2 \ll 1$, this indirect contribution should enter as a τ_2 -dependent coefficient in front of the expression for P_{RAD} for the first harmonic (see eq. [97]). In general, a transition involving the n th harmonic where $n > 1$ contributes to all the lower harmonics up to $n - 1$ via spawning. For fitting the data in Figure 9, we include just the first two harmonics, which we expect to be the dominant contributors to P_{RAD} for the range of N_e we consider. In addition, we take, for simplicity, pure constants for the coefficients for the contributions from each of these harmonics.

Thus, for the general expression for P_{RAD} , we have

$$\frac{P_{\text{RAD}}}{P_0} = \eta = 2.5 \left(\frac{T}{m_e} \right)^{1/2} \left\{ \left[\ln \left(1 + \frac{0.34\tau_1^2}{1 + 1.9\tau_1} \right) \right]^{1/2} + 2.1 \left[\ln \left(1 + \frac{0.085\tau_2^2}{1 + 1.5\tau_2} \right) \right]^{1/2} \right\}. \quad (99)$$

This function is plotted in Figure 9 for $T = 2.7, 3.6, 5.35, 8, 10.7,$ and 16 keV. The fit is good to better than 5% for all the data shown.

In Figure 10, we repeat Figure 9, but now for $E_2 = 1000$ keV. This is the radiation pressure relevant to the burst GB 880205. Because of the stronger continuum contribution, η rises more sharply at large column depths compared to the case with $E_2 = 100$ keV. (This is very apparent in Fig 7.) To construct a fitting formula for the data in Figure 10 that includes the proper physics, we need to include the (optically thin) continuum contribution. For consistency, we must then include the first three harmonics (which we follow in our model). Since the added functions and parameters are not required by the data (eq. [99], e.g., fits the data in Fig. 9 very well), we have opted here for a simple *numerical* fit to the data. We find that the function

$$\frac{P_{\text{RAD}}}{P_0} = \eta = 1.7 \left(\frac{T}{m_e} \right)^{0.3} N_{e,21}^{0.4} \quad (100)$$

fits the data in Figure 10 to better than $\sim 10\%$. This function is plotted in Figure 10.

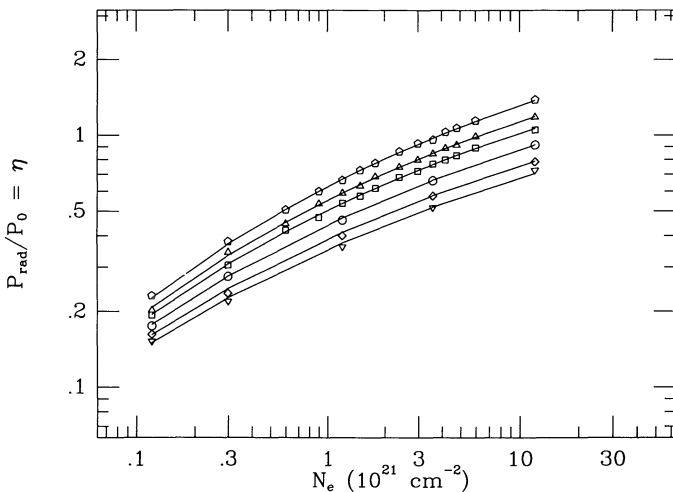


FIG. 9

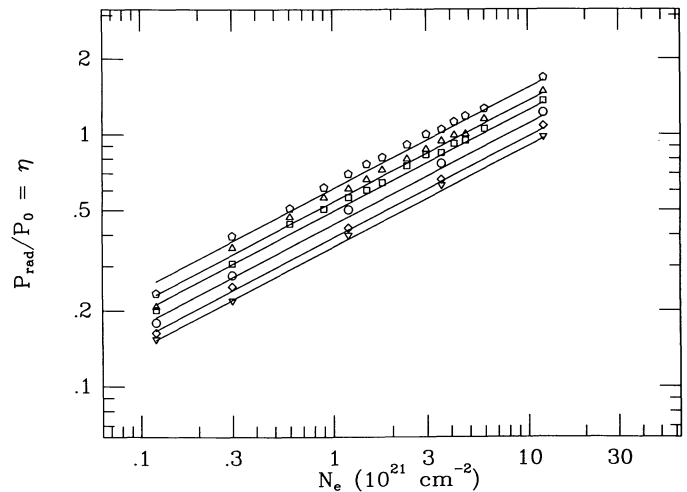


FIG. 10

FIG. 9.—The dimensionless line radiation pressure force due primarily to resonant scattering at the first three cyclotron harmonics ($E_2 = 100$ keV) as a function of N_e for $T = 2.7$ (inverted triangle), 3.6 (diamond), 5.35 ($= T_c$, circle), 8 (box), 10.7 (triangle), and 16 keV (pentagon). $B_{12} = 1.71$ for all the data. The 1σ Monte Carlo statistical errors are about the size of the symbols representing the data points and are not shown. The solid curves are given by the fitting formula in eq. (99).

FIG. 10.—The dimensionless radiation pressure force with $E_2 = 1000$ keV as a function of N_e for $T = 2.7$ (inverted triangle), 3.6 (diamond), 5.35 ($= T_c$, circle), 8 (box), 10.7 (triangle), and 16 keV (pentagon). $B_{12} = 1.71$ for all the data. The 1σ Monte Carlo statistical errors are about the size of the symbols representing the data points and are not shown. The solid curves are given by the fitting formula in eq. (100).

ii) Distance Constraint

Following the arguments given in § IIIa(i), we may calculate a distance bound and the corresponding luminosity bound for the line radiation source. We assume here that the scattering layer is an e -ion plasma that resides on or near the surface of a neutron star. We found in § IIIa(ii) that if the line-enhanced radiation force much exceeded the force of gravity binding the layer to the neutron star, the layer would be pushed out and disrupted in $\sim 10^{-5}$ s (see eq. [89]). We therefore require that $P_{\text{RAD}} < P_{\text{grav}}$ (see eq. [82]). Hereafter in our calculations, we specialize to the burst GB 880205.

Wang *et al.* (1989) and Lamb *et al.* (1989) have argued that the observed spectral dips in GB 880205 can only arise in the “transmitted” spectra of photons emerging through the *top* of a slab irradiated from *below*. (“Reflected” spectra tend to show spectral peaks, not dips.) It is an observational fact that the lines observed in this burst persist for at least a 5 s interval in the 16 s burst. A *minimal* requirement for the survival of a statistic scattering layer is that the line-enhanced radiation force on the scattering layer not exceed the force of gravity binding it to the neutron star. For an optically thick scattering layer, the radiation pressure force on the slab is given by equations (100) and (93). For GB 880205, $A_{\text{obs}} = 0.08$ photons cm^{-2} s^{-1} keV^{-1} , $E_B = 19.84$ keV ($B_{12} = 1.71$), $E_b = 101.3$ keV, and $s = 0.846$ (see eq. [59]). Requiring $P_{\text{RAD}} < P_{\text{grav}}$ then gives

$$D(\text{pc}) < 90 M_{1.4}^{1/2} \left(\frac{B_{12}}{1.71} \right)^{-0.58} \left(\frac{T}{5.35 \text{ keV}} \right)^{-0.15} y_{-3}^{0.3} f_p^{1/2} \quad (101)$$

(see eq. [83]). Using $y_{-3} = 2\mu_e$, the best-fit column depth for GB 880205, we get $D < 110\mu_e^{0.3} f_p^{1/2}$ pc for $M_{1.4} = 1$. The distance upper bound is proportional to $y_{-3}^{0.3}$ and so varies by only a factor of 4 between $y_{-3} = 0.2\mu_e$ ($55\mu_e^{0.3} f_p^{1/2}$ pc) and $y_{-3} = 20\mu_e$ ($220\mu_e^{0.3} f_p^{1/2}$ pc). These column depths delineate the approximate 3σ boundaries (in column depth) of the fits to GB 880205 by Wang *et al.* (1989).

The distance constraint, equation (101), is only weakly dependent on E_2 since the line-enhanced radiation force depends only weakly on the continuum (see § IIIb[i], Fig. 7). Our simulations were run for isotropic photon injection, so it is not possible for us to extrapolate the results to other modes of injection. However, angular redistribution associated with resonant scattering should, if anything, decrease the dependence of the distance constraint on the angular distribution of the incident continuum (cf. § IIIa[i]). However, for incident photons that are beamed along the magnetic field, the component of the force due to higher harmonic transitions will be suppressed. The $n = 2$ spectral feature in GB 880205 (Murakami *et al.* 1988; Fenimore *et al.* 1988) suggests that the incident continuum is not strongly peaked parallel to the field in this source.

From the distance constraint, we also infer that the total hard X-ray luminosity of GB 880205 at $1 \text{ keV} < E < 1000 \text{ keV}$ is sub-Eddington. Thus, using equations (59), (45), and (101), we have

$$L \leq 4\pi R^2 F_E^{\text{loc}} = 4\pi R^2 \int_{1 \text{ keV}}^{1000 \text{ keV}} dE E N_{\text{loc}}(E) < \left[0.06 \left(\frac{B_{12}}{1.71} \right)^{-1.16} \left(\frac{T}{5.35 \text{ keV}} \right)^{-0.3} y_{-3}^{0.6} \right] L_E \quad (102)$$

(see eq. [84]). The right-hand side of equation (102) is the *magnetic* Eddington luminosity for optically thick media for our model. Note that this limiting luminosity is independent of f_p (see eq. [84]).

In equation (102), L_E is the Eddington luminosity appropriate for an e - p plasma. For a pair (e^+e^-)-dominated plasma (i.e., $n_{e^+}/n_p \gg 1$), the Eddington luminosity is $\sim m_p/m_e = 1836$ times smaller than that given in equation (85). To accommodate a sub-Eddington pair-dominated plasma in our model requires placing the burst GB 880205 at $D \lesssim 5$ pc, which seems highly unlikely (Hartmann, Epstein, and Woosley 1990; Paczynski 1990).

Our distance bound (eq. [101]) also implies an upper bound to the photon *number* flux at the γ -ray source,

$$\mathcal{N} = f_a 4\pi R^2 F_N^{\text{loc}} = f_a 4\pi R^2 \int_{1 \text{ keV}}^{1000 \text{ keV}} dE N_{\text{loc}}(E) < 3.9 \times 10^{43} M_{1.4} \left(\frac{B_{12}}{1.71} \right)^{-1.16} \left(\frac{T}{5.35 \text{ keV}} \right)^{-0.3} y_{-3}^{0.6} f_a \text{ s}^{-1}. \quad (103)$$

For comparison, the blackbody number flux emitted from an area of size $\Delta\Omega R^2$ at temperature T_{BB} is

$$\mathcal{N}_{\text{BB}} = 3.0 \times 10^{45} \left(\frac{T_{\text{BB}}}{\text{keV}} \right)^3 R_{10}^2 f_a \text{ s}^{-1}, \quad (104)$$

where $f_a = \Delta\Omega/4\pi$ and $R = 10R_{10}$ km. Setting $\mathcal{N} = \mathcal{N}_{\text{BB}}$ in equation (103), we obtain an upper bound on the equivalent blackbody “number” temperature of the radiation from GB 880205 between 1 keV and 1 MeV:

$$T_{\text{BB}} < 0.2 R_{10}^{-2/3} M_{1.4}^{1/3} \left(\frac{B_{12}}{1.71} \right)^{-0.39} \left(\frac{T}{5.35 \text{ keV}} \right)^{-0.1} y_{-3}^{0.2} \text{ keV}. \quad (105)$$

Thus, if GB 880205 is located at $D \lesssim 200$ pc, then its total hard X-ray photon *number* flux at $1 \text{ keV} < E < 1000 \text{ keV}$ is comparable to that from a blackbody at temperature $\lesssim 0.3$ keV. This is suggestive of the possibility that the γ -ray burst arises due to some transient phenomenon that triggers the production of high-energy electrons (Blaes *et al.* 1989; Melia 1990*a, b*; Ho and Epstein 1989; Dermer 1989, 1990) which Compton upscatter the soft photon background to produce a burst of high-energy γ -rays. Since scattering conserves photon number, the number flux of the high-energy photons in the burst is the same as the soft photon number flux. Interestingly, Murakami (1988) reports that the late time flux in the burst GB 870303 can be fitted by a blackbody at a temperature ~ 1 keV.

IV. CONCLUSIONS

In this paper, we have investigated, in both the optically thin ($\tau_1 \ll 1$) and thick ($1 \lesssim \tau_1 \lesssim 1/a$) cases, the cooling and heating arising from cyclotron resonant and nonresonant (magnetic continuum) scattering. We find that the equilibrium temperature resulting from a balance of the cooling and heating due to resonant scattering is $\sim E_B$ and is fairly independent of depth up to $N_e \approx 6 \times 10^{21}$ electrons cm^{-2} (see Fig. 5). The extra heating due to the continuum drives the equilibrium temperature above the pure line value (see Fig. 5), thereby limiting the extent of the line-dominated layer. With an injection spectrum $\sim 1/E$ up to $E_2 \sim 2m_e$, and $B_{12} \sim 2$, the thickness of the line-dominated layer $\sim 10^{21}$ – 10^{22} electrons cm^{-2} . The thickness decreases for increasingly hard incident spectra (see Fig. 5, eq. [70]).

We have also studied, in both the optically thin and thick cases, the line-enhanced radiation pressure force acting on the slab electrons in the direction of the field (parallel to the slab normal). If we assume that the scattering layer is gravitationally bound and ion-dominated, then we can derive distance and luminosity bounds for γ -ray bursts by requiring that the radiation pressure force on the line-forming region not exceed the gravitational force per unit area (along the field in our model) (see eqs. [83], [84], [101], [102]). The luminosity bound, or magnetic Eddington limit, is ~ 0.01 the nonmagnetic Eddington luminosity when $\tau_1 \ll 1$, and increases as τ_1 increases.

Our optically thick analysis may be directly applied to the burst GB 880205. From the current work and that of Wang *et al.* (1989), we believe we have at least a qualitative physical understanding of the three fitted parameters (B , T , N_e) needed to model the line-forming scattering layer in this burst. To summarize: (1) the teragauss field ($\sim 2 \times 10^{12}$ G) is naturally explained as originating from or near the surface of a neutron star. (2) The low temperature (~ 5 keV) is the equilibrium temperature that results from balancing cooling and heating due primarily to *resonant* cyclotron scattering at the first harmonic (=fundamental). (3) The thickness of the line-forming layer derived from the fits is of the same order of magnitude as the thickness of the cool layer where lines dominate the energy balance. This coincidence *suggests* that the cool line-dominated layer plays an important role in the line formation process. Our one-zone models, however, do not allow us to rigorously establish a connection between the line-dominated region and the line-forming region. To do this, and in particular, to determine the relationship (if any) between the thickness of these two regions requires a study of the spectral evolution through a multizone (nonisothermal) atmosphere where the temperature is determined self-consistently from physical processes such as electron-photon scattering. This is the next step in our analysis. (4) The line-enhanced radiation force on the scattering layer gives a distance constraint $D \lesssim 200$ pc (3σ bound) for GB 880205, which implies a total hard X-ray luminosity $L \lesssim 0.3L_E$. This constraint is calculated based on a well-understood physical process—electron-photon scattering. The line-forming region is probably not pair-dominated because in our model this would give a very low distance bound ($\lesssim 5$ pc), which seems highly unlikely. Both the cyclotron interpretation of the line features and the 200 pc distance limit strongly suggest that the burst GB 880205 originated from a neutron star in the Galactic disk.

It is a pleasure to thank Jim Brainerd and Tom Loredo for valuable discussions. J. C. L. W. acknowledges the gracious hospitality of the Department of Astronomy at Cornell University where part of this work was completed. J. C. L. W. also acknowledges the support of a Robert R. McCormick Postdoctoral Fellowship from the University of Chicago. This work was supported in part by NASA grants NAGW-830 and NAGW-1284 to the University of Chicago and NAGW-666 to Cornell University and NSF grant AST-89-13112 to Cornell University. We acknowledge the National Center of Supercomputing Applications at Urbana and the Cornell National Supercomputing Facility where the computations were done.

APPENDIX A

THE MAGNETIC AND NONMAGNETIC Λ_{cont} , Γ_{cont} , T_C^{cont} , AND $(\delta p/\delta t)_{\text{cont}}$

Substituting equation (31) for $N_{\text{loc}}(E)$ into equations (37), (38), and (87) gives

$$\Lambda_{\text{cont}} = \frac{8}{15} n_e \sigma_T \left(\frac{T}{m_e} \right) A_{\text{loc}} E_b^2 I_C, \quad (\text{A1})$$

$$\Gamma_{\text{cont}} = \frac{2}{15} \frac{n_e \sigma_T}{m_e} A_{\text{loc}} E_b^3 I_H, \quad (\text{A2})$$

$$\left(\frac{\delta p}{\delta t} \right)_{\text{cont}} = \sigma_T A_{\text{loc}} E_b^2 I_F, \quad (\text{A3})$$

where

$$I_C = \int_{x_1}^{x_2} dx x^{1-s} \left[1 + \frac{4x^2}{(x+\xi)^2} + \frac{2x^2\xi}{(x+\xi)^3} \right], \quad (\text{A4})$$

$$I_H = \int_{x_1}^{x_2} dx x^{2-s} \left[1 + \frac{4x^2}{(x+\xi)^2} \right], \quad (\text{A5})$$

$$I_F = \frac{1}{4} \int_{x_1}^{x_2} dx x^{1-s} \left[1 + \frac{3x^2}{(x+\xi)^2} \right], \quad (\text{A6})$$

and $x_1 \equiv E_1/E_b$, $x_2 \equiv E_2/E_b$, $\xi \equiv E_B/E_b$.

The integrals in equations (A4)–(A6) have the form

$$\int \frac{x^m dx}{(x + \xi)^n},$$

and

$$\int \frac{dx}{x^m(x + \xi)^n},$$

where $m \geq 0$ and $n = 2, 3$. Assuming integer s and making repeated use of equations (2.153) and (2.155) in Gradshteyn and Ryzhik (1980, pp. 66–67), these integrals reduce to the following cases:

$m \geq 0$:

$$\int \frac{x^m dx}{(x + \xi)^2} = -\frac{x^m}{x + \xi} + (-)^{m-1} m \xi^{m-1} \ln(x + \xi) - m \sum_{i=1}^{m-1} (-)^i \frac{x^{m-i}}{m-i} \xi^{i-1}. \quad (\text{A7})$$

$m \geq 1$:

$$\int \frac{dx}{x^m(x + \xi)^2} = \frac{1}{\xi} \frac{1}{x^{m-1}} \frac{1}{(x + \xi)} + (-)^{m-1} \frac{m}{\xi^{m+1}} \ln\left(\frac{x}{x + \xi}\right) + (1 - \delta_{m,1}) \frac{m}{\xi} \sum_{i=1}^{m-1} \frac{(-)^i}{m-i} \frac{1}{x^{m-i}} \frac{1}{\xi^i}. \quad (\text{A8})$$

$m \geq 0$:

$$\int \frac{x^m dx}{(x + \xi)^3} = -\frac{1}{2} \frac{x^m}{(x + \xi)^2} - \frac{m}{2} \frac{x^{m-1}}{x + \xi} + (-)^m \frac{m(m-1)}{2} \xi^{m-2} \ln(x + \xi) + \frac{m(m-1)}{2} \sum_{i=2}^{m-1} (-)^i \frac{x^{m-i}}{m-i} \xi^{i-2}. \quad (\text{A9})$$

$m \geq 1$:

$$\int \frac{dx}{x^m(x + \xi)^3} = \frac{1}{2\xi} \frac{1}{x^{m-1}} \frac{1}{(x + \xi)^2} + \frac{m+1}{2\xi^2} \frac{1}{x^{m-1}} \frac{1}{x + \xi} + (-)^{m-1} \frac{m(m+1)}{2\xi^{m+2}} \ln\left(\frac{x}{x + \xi}\right) + (1 - \delta_{m,1}) \frac{m(m+1)}{2\xi^2} \sum_{i=1}^{m-1} \frac{(-)^i}{m-i} \frac{1}{x^{m-i}} \frac{1}{\xi^i}. \quad (\text{A10})$$

Hereafter, we assume $x_2 \gg \xi \gg x_1$.

Equation (A4) then simplifies to the following cases:

$$I_C \approx \begin{cases} 5 \frac{x_2^{2-s}}{2-s}, & s < 2; \\ \ln \left[\left(\frac{E_2}{E_1} \right) \left(\frac{E_2}{E_B} \right)^4 e^{-3} \right], & s = 2; \\ \frac{1}{s-2} \frac{1}{x_1^{s-2}}, & s > 2; \end{cases} \quad (\text{A11})$$

where $e = 2.7182818 \dots$

Equation (A5) has the following cases:

$$I_H \approx \begin{cases} 5 \frac{x_2^{3-s}}{3-s}, & s < 3; \\ \ln \left[\left(\frac{E_2}{E_1} \right) \left(\frac{E_2}{E_B} \right)^4 e^{-4} \right], & s = 3; \\ \frac{1}{s-3} \frac{1}{x_1^{s-3}}, & s > 3. \end{cases} \quad (\text{A12})$$

Equation (A6) has the following cases:

$$I_F \approx \begin{cases} \frac{x_2^{2-s}}{2-s}, & s < 2; \\ \frac{1}{4} \ln \left[\left(\frac{E_2}{E_1} \right) \left(\frac{E_2}{E_B} \right)^3 e^{-3} \right], & s = 2; \\ \frac{1}{4} \frac{1}{s-2} \frac{1}{x_1^{s-2}}, & s > 2. \end{cases} \quad (\text{A13})$$

Equations (A11)–(A13) are valid for all real s .

Equating Λ_{cont} and Γ_{cont} gives the equilibrium Compton temperature, $T_{\text{C}}^{\text{cont}}$, due solely to magnetic continuum scattering

$$T_{\text{C}}^{\text{cont}} = \frac{1}{4} \frac{I_{\text{H}}}{I_{\text{C}}} E_b .$$

From equations (A11) and (A12), we have

$$T_{\text{C}}^{\text{cont}} \approx \begin{cases} \left[\frac{1}{2} \left(\frac{2-s}{3-s} \right) \frac{E_2}{2m_e} \right] m_e , & s < 2 ; \\ \left\{ \frac{5/2(E_2/2m_e)}{\ln [(E_2/E_1)(E_2/E_B)^4 e^{-3}]} \right\} m_e , & s = 2 ; \\ \left\{ \frac{E_1}{2m_e} \ln \left[\left(\frac{E_2}{E_1} \right)^{1/2} \left(\frac{E_2}{E_B} \right)^2 e^{-2} \right] \right\} m_e , & s = 3 ; \\ \left[\frac{1}{2} \left(\frac{s-2}{s-3} \right) \frac{E_1}{2m_e} \right] m_e , & s > 3 . \end{cases}$$

Note that unlike the resonant scattering case (see eq. [50]–[53]), the continuum Compton temperature exists for all s .

In nonmagnetic ($B = 0$) continuum scattering, if the (three-dimensional) electron distribution is isotropic or if distribution is isotropic, then the cooling and heating rates are given to leading order in β^2 and E/m_e by

$$\Lambda_{\text{cont}}(B = 0) = 4n_e \sigma_{\text{T}} \left(\frac{T}{m_e} \right) \int_{E_1}^{E_2} dE E N(E) ,$$

and

$$\Gamma_{\text{cont}}(B = 0) = \frac{n_e \sigma_{\text{T}}}{m_e} \int_{E_1}^{E_2} dE E^2 N(E) .$$

To do a direct comparison with the magnetic results, we assume the photon flux is emitted isotropically into a scattering near the surface of a neutron star so that we may use equation (30) to relate $N(E)$ to $N_{\text{loc}}(E)$. Taking equation (31) for N_{loc}

$$\Lambda_{\text{cont}}(B = 0) = 8n_e \sigma_{\text{T}} \left(\frac{T}{m_e} \right) A_{\text{loc}} E_b^2 \times \begin{cases} \frac{x_2^{2-s}}{2-s} , & s < 2 ; \\ \ln \left(\frac{E_2}{E_1} \right) , & s = 2 ; \\ \frac{1}{s-2} \frac{1}{x_1^{s-2}} , & s > 2 ; \end{cases}$$

and

$$\Gamma_{\text{cont}}(B = 0) = 2 \frac{n_e \sigma_{\text{T}}}{m_e} A_{\text{loc}} E_b^3 \times \begin{cases} \frac{x_2^{2-s}}{3-s} , & s < 3 ; \\ \ln \left(\frac{E_2}{E_1} \right) , & s = 3 ; \end{cases}$$

Equating equations (A16) and (A17) gives the nonmagnetic Compton temperature. Taking $N(E) \propto E^{-s}$ gives

$$T_C^{\text{cont}}(B=0) = \begin{cases} \left[\frac{1}{2} \left(\frac{2-s}{3-s} \right) \frac{E_2}{2m_e} \right] m_e, & s < 2; \\ \left\{ \frac{(E_2/2m_e)/4}{\ln(E_2/E_1)^{1/2}} \right\} m_e, & s = 2; \\ \left[\left(\frac{E_1}{2m_e} \right) \ln \left(\frac{E_2}{E_1} \right)^{1/2} \right] m_e, & s = 3; \\ \left[\frac{1}{2} \left(\frac{s-2}{s-3} \right) \frac{E_1}{2m_e} \right] m_e, & s > 3. \end{cases}$$

Consider a local xyz -coordinate system with the electron at the origin. With photons injected along the $+z$ - xy -plane, the component of force along the z -direction owing to ordinary Thomson scattering is simply

$$\left(\frac{\delta p}{\delta t} \right)_{\text{cont}}(B=0) = \sigma_T F_E^{\text{loc}},$$

where

$$F_E^{\text{loc}} = \int_{E_1}^{E_2} dE E N_{\text{loc}}(E).$$

Taking equation (31) for $N_{\text{loc}}(E)$ and assuming $E_2 \gg E_1$ gives

$$F_E^{\text{loc}} = A_{\text{loc}} E_b^2 \times \begin{cases} \frac{x_2^{2-s}}{2-s}, & s < 2; \\ \ln \left(\frac{E_2}{E_1} \right), & s = 2; \\ \frac{1}{s-2} \frac{1}{x_1^{s-2}}, & s > 2. \end{cases}$$

For $s < 2$, the force is the same as its magnetic counterpart (see eqs. [A3] and [A13]). This is because in both the nonmagnetic cases, unlike cooling and heating, only one dimension is active, i.e., $(\delta p/\delta t)_{\text{cont}}$ is the projection of the dimension. For $s > 2$, the magnetic force is weaker owing to the reduced cross section at the dominant low photon energy.

REFERENCES

- Blaes, O., Blandford, R., Goldreich, P., and Madau, P. 1989, *Ap. J.*, **343**, 839.
 Buneman, O. 1959, *Phys. Rev.*, **115**, 503.
 Dermer, C. D. 1989, *Ap. J. (Letters)*, **347**, L13.
 ———. 1990, *Ap. J.*, **360**, 197.
 Fenimore, E. E., et al. 1988, *Ap. J. (Letters)*, **335**, L71.
 Gnedin, Yu. N., Pavlov, G. G., and Shibano, Yu. A. 1978, *Soviet Astr. Letters*, **4**, 117.
 Gradshteyn, I. S., and Ryzhik, I. M. 1980, *Table of Integrals, Series, and Products* (Orlando: Academic).
 Hartmann, D., Epstein, R. I., and Woosley, S. E. 1990, *Ap. J.*, **248**, 625.
 Ho, C., and Epstein, R. I. 1989, *Ap. J.*, **343**, 277.
 Lamb, D. Q., Wang, J. C. L., Lored, T. J., Wasserman, I. M., and Fenimore, E. E. 1989, in *Proc. 14th Texas Symposium on Relativistic Astrophysics*, ed. E. Fenyves (New York: Ann NY Acad. Sci.), **571**, 460.
 Mazets, E. P., and Golenetskii, S. V. 1981, *Astr. Space Sci.*, **75**, 47.
 Melia, F. 1990a, *Ap. J.*, **351**, 601.
 ———. 1990b, *Ap. J.*, **357**, 161.
 Mitrofanov, I. G., and Pavlov, G. G. 1982, *M.N.R.A.S.*, **200**.
 Murakami, T. 1988, in *Physics of Neutron Stars and Black Holes* (Tokyo: Universal Academy Press), p. 405.
 Murakami, T., et al. 1988, *Nature*, **335**, 234.
 Paczyński, B. 1990, *Ap. J.*, **348**, 485.
 Rybicki, G. B., and Lightman, A. P. 1979, *Radiative Processes* (New York: Wiley).
 Shapiro, S. L., and Teukolsky, S. A. 1983, *Black Holes, Neutron Stars: The Physics of Compact Objects* (New York: Wiley).
 Ventura, J. 1973, *Phys. Rev. A*, **8**, 3021.
 Wang, J. C. L., and Lamb, D. Q. 1989, *Ap. J.*, submitted.
 Wang, J. C. L., et al. 1989, *Phys. Rev. Letters*, **63**, 1550.
 Wang, J. C. L., Lamb, D. Q., Lored, T. J., Wasserman, I. M., and Fenimore, E. E. 1990, *Ap. J.*, in preparation.
 Wang, J. C. L., Wasserman, I. M., and Salpeter, E. E. 1980, *Ap. J.*, **241**, 1107.